Title: Longitudinal analysis of matched patient biospecimens reveals Neural Reprogramming of Cancer-Associated Fibroblasts Following Chemotherapy in Pancreatic Ductal Adenocarcinoma

Aylin Z. Henstridge[1]; Nandini Arya[2]; Ahmed M. Elhossiny[3]; Padma Kadiyala[4]; Georgina Branch[2]; Vaibhav Sahai[5,6,7]; Nicole Peterson[5]; Jorge Machicado[2]; Richard Kwon[2]; Allison Schulman[2]; Erik Wamsteker[2]; George Philips[2,8]; Stacy Menees[2,8]; Jonathan Xia[2], Arvind Rao[3,5,9], Jiaqi Shi[6,7,10]; Timothy Frankel[4,6,7,]; Filip Bednar[1,4,6,7]; Marina Pasca di Magliano[1,4,6,7,11]; Costas A. Lyssiotis[1,2,6,7,12]; Mark Truty[13]; Martin Fernandez-Zapico[14]; Eileen S. Carpenter[1,2,6, 7, 8,]

[1]Cancer Biology Graduate Program, University of Michigan, Ann Arbor, MI
[2]Department of Internal Medicine, Division of Gastroenterology, University of Michigan, Ann Arbor, MI
[3]Department of Computational Medicine and Bioinformatics, University of Michigan, Ann Arbor, MI
[4]Departmeny of Surgery, University of Michigan, Ann Arbor, MI
[5]Department of Internal Medicine, Division of Hematology and Oncology, University of Michigan, Ann Arbor, MI
[6]Rogel Cancer Center, University of Michigan, Ann Arbor, MI.
[7]Rogel and Blondy Center for Pancreatic Cancer, University of Michigan, Ann Arbor, MI
[8]Division of Gastroenterology, Veterans Affairs Health System, Ann Arbor, MI
[9]Department of Radiation Oncology, University of Michigan, Ann Arbor, MI
[10]Department of Pathology, University of Michigan, Ann Arbor, MI
[11]Department of Cell and Developmental Biology, University of Michigan, Ann Arbor, MI
[12]Department of Molecular and Integrative Physiology, University of Michigan, Ann Arbor, MI
[13]Department of Hepatobiliary and Pancreas Surgery, Mayo Clinic, Rochester, MN
[14]Division of Oncology Research, Department of Oncology, Mayo Clinic, Rochester, MN
Correspondence: Dr. Eileen Carpenter, Medical Science Building II, Room 7712A, University of Michigan 1137 Catherine St, Ann Arbor, MI 48109. Email: eicarpen@med.umich.edu. Telephone 734-615-3948

Disclosures:
A.R consults for Tempus and Telperian. He also serves as member for Voxel Analytics, LLC; an affiliate investigator for the Fred Hutch Cancer Center, and a Satish Dhawan Visting Chair Professor at the Indian Institute of Science, Bangalore India. A.S reports the following disclosures: Apollo Endosurgery - Consultant, Advisory Board, Boston Scientific – Consultant, Olympus – Consultant, MicroTech – Consultant, GI Dynamics - Research / grant support, Fractyl - Consultant, Research / grant support. VS reports the following disclosures: Institutional research grant funding – Actuate Therapeutics, Boehringer Ingram, Bristol-Myers Squibb, Clovis, Elicio, Esanik, Exelixis, Fibrogen, Jazz, Ipsen, NCI, PanCAN, Cornerstone (previously Rafael), Relay, Repare, Servier, Transthera, Consultant – AstraZeneca, Autem, Amplity (previously Lynx Group), Delcath, Elevar, HistoSonics, Incyte, Ipsen, Jazz, Servier, Tallac, TransThera, Provision of equipment/supplies – Cornerstone (previously Rafael), Travel/lodging – Japanese Society of Clinical Oncology, BinayTara Foundation, Cholangiocarcinoma Foundation, HistoSonics, Lynx Group/Amplity, NCCN, Chinese Association of Pancreatology. The rest of the authors report no relevant disclosures.

Abstract

Pancreatic ductal adenocarcinoma (PDAC) has poor response to chemotherapy with a strong likelihood of recurrence. While previous studies have examined patient samples collected before and after chemotherapy, few have analyzed matched samples from the same patients to allow for deconvolution of interpatient heterogeneity, a large limitation to PDAC studies. Here, we study the effects of chemotherapy on the tumor microenvironment using scRNA sequencing of matched pre- and post- treatment tissue biopsies from 5 patients. While immune subsets were heterogeneously affected by chemotherapy treatment, we found near-universal enrichment of axonal guidance genes in cancer associated fibroblasts (CAFs) post-treatment. We validated the *in-situ* expression of these genes in patient-derived PDAC tissues and observed that these neural CAFs localized near regions of perineural invasion, where tumor cells had increased proliferation. Furthermore, predicted ligand-receptor interactions between these CAFs and tumor cells further predicts that these CAFs have the potential to drive tumor progression.

Introduction

Pancreatic ductal adenocarcinoma (PDAC) is a deadly disease and will be the second leading cause of cancer related death by 2030.[1] Diagnosis usually occurs at advanced stages of disease, making surgical resection available to only 15-20% of patients.[2] The mainstays of therapy are cytotoxic treatment consisting of either FOLFIRINOX(5-Fluoroacil, irinotecan, leucovorin, and oxaliplatin) or gemcitabine/nab-paclitaxel, although patients eventually progress due to chemoresistance, leading to poor outcomes.[3] Even in the case of surgical resection and chemotherapy, recurrence is common with a median overall survival of less than 2 years. Thus, there is an urgent need to elucidate mechanisms of therapeutic resistance to develop better strategies for treatment.

Past studies have looked at pre-and post-treatment samples in an unmatched context and have attempted to characterize the changes in the tumor and its surrounding microenvironment in response to treatment[4–6], however, substantial interpatient heterogeneity continues to complicate findings. Despite progress, comprehensive studies exploring chemotherapy's impact on the tumor microenvironment using matched samples—thereby controlling for patient-specific variability—remain limited and remain a challenging feat as methods to obtain pancreatic tumor tissue are resource-intensive and not without risk. We have overcome this obstacle by exploiting the endoscopic opportunity to obtain treatment naïve fine needle biopsy specimens during diagnostic biopsy and matched post-treatment specimens at time of endoscopic fiducial placement or at surgical resection.

Here, we study the effects of chemotherapy on five matched patient tumors using sc-RNA sequencing sampled longitudinally before and after treatment. While the changes in the immune microenvironment were widely heterogenous, interestingly, there was a consistent theme in that cancer associated fibroblasts (CAFs) displayed enrichment of neural axonal guidance programs following treatment. These findings have important clinical implications given the hallmark of perineural invasion as a pathogenic process in PDAC[7–9] and the growing field of cancer neuroscience investigating the role of peripheral nervous system (PNS) neurons as active members of the tumor microenvironment.

Results

Sc-RNA Sequencing of five matched patients pre- and post-chemotherapy reveals a diverse tumor microenvironment with transcriptomic variability

In order to study the effects of chemotherapy in PDAC patients, we collected longitudinal biospecimens from 5 patients by leveraging endoscopic fine-needle biopsy obtained during diagnostic workup. Following treatment with chemotherapy, we obtained biospecimens from either endoscopic fine needle biopsies taken during endoscopic procedures performed for clinical care (fiducial placement) or procured tumor tissue from surgical resection(Figure 1A and 1B). The post-treatment sample for all patients were collected at least 4-weeks after the conclusion of any chemotherapy treatment. Of note, patient 1475 was additionally sampled at a third time point for tumor recurrence. This sample was taken 13 months after total pancreatectomy (Figure 1A, B). The cohort was heterogeneous, both in terms of the treatment received (Figure 1B), and treatment response (Figure 1C and Supplemental Table 1A).

To parse the cell-specific differences with treatment, utilizing single-cell RNA sequencing, epithelial, immune, and stromal cell clusters were manually identified using known gene signatures (Figure 1E). Pseudobulk analysis revealed broad transcriptomic differences between treatment naïve and post-treatment samples across all cell types (Supplemental Figure 1A), with no observable trends in cell type frequency across samples(Supplemental Figure 1B). We thus turned our focus to patient- and cell-type specific differences to parse out the effects of chemotherapy treatment.

Tumor epithelial compartment is largely undetectable in treated PDAC specimens by single cell RNA sequencing

Utilizing the *Numbat*[10] pipeline, which leverages allelic frequences and gene expression frequency to estimate copy number alteration, we identified the cells in our population that had a high probability of being malignant

epithelial cells (Figure 1F). Upon observation of these proportions on a patient-specific level, it was determined that the tumor epithelial content of the biopsies post-treatment was too low to sufficiently analyze changes in gene expression. This was likely due to the intended cytotoxic effects of chemotherapy (Figure 1G). The lack of malignant epithelial cells post-treatment was further corroborated by the clinical pathologist examination of samples (Supplementary Table 1A, Figure 1C).

CXCR4 is unanimously enriched CD8+ T-cells post-treatment, with increased interactions between T-cells and cancer associated fibroblasts

Given the hallmark immunosuppressive environment of PDAC, characterized by abundant myeloid infiltration and relatively sparse cytotoxic T cells[11,12] we next examined the immune microenvironment in our dataset. Upon subtyping the T-Cell population, we identified a variety of CD8+ and CD4+ T-Cells, as well as NK and NKT Cells (Figure 2A), which were identified utilizing genes published in literature (Figure 2B)[13]. We first queried whether there were changes in individual cell frequencies to identify if immune sub-populations were positively or negatively affected by treatment and found a decrease in NK Cells after chemotherapy (Supplementary Figure 1C). Querying known markers of immune activation and exhaustion within the T cell compartments for each patient, we found that *TIGIT* expression in CD8+ T-cells, which we and others[4,12,14] have previously reported to be expressed in tumor-infiltrating T-cells in PDAC, decreased after treatment in a subset of patients (Figure 2C). The decrease in TIGIT was primarily driven in exhausted CD8+ T-Cells (Supplementary Figure 1D) and correlated clinically, with TIGIT levels decreasing in patients with good treatment response and resectable disease (1471/1529) while remaining unchanged in those that had worse clinical outcomes (1475/1550/1402) (Figure 1A). We did identify, however, one unanimous change in that there was an increase in *CXCR4* expression in the CD8+ T-cells of all patients and the CD4+ T cells of most patients post-chemotherapy (Figure 2C, D). Among the subpopulation of CD8+ and CD4+ T-Cells, CXCR4 was enriched in all cytotoxic and exhausted CD8 T-Cells and regulatory T-cells, with the steepest increase seen in cytotoxic CD8+ T-Cells (Supplementary Figure 1D). *CXCR4* expression has been implicated in T-Cell exhaustion, and *CXCR4* antagonists have been recommended in other PDAC to sensitize the tumor to immunotherapy regimens such as PD-1 checkpoint inhibitors.[15]

To understand the role of CXCR4 in the context of treatment, we used the CellChat V2 pipieline[16] to look at inferred ligand-receptor interaction strength and specifically queried chemokine signaling in the immune-stromal compartment. We identified a post-treatment increase in *CXCL12-CXCR4* interactions between CAFs and both CD8+ and CD4+ T-cells (Figure 2E, F). We simultaneously observed an increase in *CXCL12* expression in our CAF population. Of note, *CXCR4* was not found to be appreciably expressed in CAFs in our cohort (Figure 2E). CAF-secreted *CXCL12* has been shown to play an important role in tumor microenvironment crosstalk previously[17] and these data indicate that this crosstalk may be enhanced after chemotherapy treatment. Recently it was reported that *CXCR4* expressing plasma cells interact with *CXCL12* expressing myofibroblasts, leading to the exclusion of plasma cells from the tumor microenvironment; the interaction between *CXCL12*+ CAFs and *CXCR4*+ T-cells could further this immunosuppressive activity.[17]

In addition to the T-Cells, we also examined the Myeloid cell population, which contained subsets of macrophages, granulocytes, and dendritic cells (Figure 2G-H). We found an increase in alternatively activated macrophages with chemotherapy, marked by *C1QA, APOE*, and *SPP1* – a population which we previously reported to be important for establishing the premetastatic niche (Figure 2G).[18] We also identified a decrease in *CCR1-CCL5* signaling between macrophages and T-cells/NK cells (Figure 2F). This pathway in macrophages has been associated with increased drug resistance, invasiveness, tumor growth and promotes the further polarization of macrophages to a tumor-promoting and immunosuppressive subtype.[19] Altogether, these proposed interactions indicate that chemotherapy may impact different cell populations within the tumor microenvironment in diverse ways—potentially driving context-dependent tumor-promoting and tumor-inhibiting effects.

An 'axonal guidance' gene signature is enriched in a sub-population of CAFs following treatment

The rich population of CAFs in the PDAC tumor microenvironment, and the increase in CAF-derived *CXCL12* with therapy prompted us to further examine the CAFs in our dataset. This yielded 3 distinct clusters of CAFs

which we termed Fibro1, Fibro2 and Fibro3 (Figure 3A). The proportions of these groups of CAFs were relatively stable between timepoints within each patient, barring a few changes in specific patient timepoints (Figure 3B). The top expressed genes in all three clusters involved canonical CAF genes (*α-SMA, PDGFRα, TAGLN*), with *CXCL12* identified predominately in Fibro1 and Fibro2 (Figure 3C). Interestingly, the top expressed genes in Fibro3 were involved in axonal guidance and neurite outgrowth (*NEGR1, SLIT2, NRP1*) (Figure 3C, D). In order to better understand the varying sub-groups of CAFs, we applied published myofibroblast (myCAF), inflammatory fibroblast (iCAF), and antigen-presenting fibroblast (apCAF) gene signatures (Figure 3E).[20] The myCAF gene signature was predominately expressed in Fibro2, whereas iCAF relevant genes were predominantly expressed in Fibro1. apCAF genes were identified in a few individual cells across Fibro1 and Fibro2, with very minimal expression. Fibro3, as expected, displayed enrichment of axonal guidance genes distinct from the aforementioned CAF subtypes (Figure 3C, D ,E). We thus developed a 7-gene NR-CAF signature consisting of axonal guidance genes (*NEGR1, SLIT2, ROBO1, SEMA3A, NRP1, NFIA,* and *EPHA3*) (Figure 3E). We thus referred to fibroblasts enriched for our derived NR-CAF signature neural gene positive CAFs (NR+ CAFs) (Figure 3E). From our pseudobulk analysis, we observed that CAFs displayed wide heterogeneity pre-treatment but converged transcriptomically post-treatment (Supplementary Figure 2A). To further investigate changes at a patient-specific level, we queried each component of the NR-CAF signature, which was observed to be increased post-treatment in almost every patient (Figure 3F). Additionally, we saw the opposite trend with *ACTA2*, suggesting a decrease in myCAFs after chemotherapy treatment, as well as shifts in common fibroblast gene markers (Figure 3F). Specifically, *FAP* and *LRRC15*[21,22], both associated with immunosuppression in the tumor microenvironment, was decreased following treatment, while DPT, a pan-fibroblast marker which we had previously found to be expressed variably across fibroblast populations[23], was increased. We observed an enrichment in fibroblast marker *DPT* and a decrease in *LRRC15* and *FAP.* Increases in *PDGFRA* and *TAGLN*, along with decreases in *PDGFRB* and *PDPN* were also observed (Supplementary 2B). We further compared myCAF and iCAF gene signatures patient-by-patient across treatment groups and saw heterogenous increases and decreases in both populations in each patient with a dominant trend of decreased myCAF expression. Compared to this heterogeneity, we saw a near unanimous trend in increased NR-CAF expression (Figure 3G). Patient 1529 was consistently an outlier to this trend, but it is worth noting that this patient had displayed the best response to treatment out of the cohort (Figure 1A, Supplemental Table 1A). To query the NR-CAF signature with a larger CAF dataset, we merged our data with our previously published dataset which included healthy pancreatic tissue, adjacent normal pancreatic tissue, and untreated PDAC tumor samples [23] Subsetting out the PDAC CAFs in this merged dataset, we mapped the (NR+) CAFs and identified that they not only were present in this dataset but grouped together with little overlap to the myCAF population (Figure 3H, I). Notably, with the inclusion of more treatment-naïve samples, enrichment of the NR-CAF signature was still present post-treatment (Figure 3J). Overall, we observed that chemotherapy exerts diverse changes the immune microenvironment in PDAC while consistently promoting the upregulation of neuronal axon guidance genes in CAFs.

The NR-CAF signature is partially recapitulated in the absence of malignancy.

To expand our understanding of the NR-CAF signature, we further queried the expression of these genes in fibroblasts of the healthy pancreas using donor pancreata. To do this, we extracted the healthy CAFs from our merged dataset. Upon comparing healthy pancreatic fibroblasts and PDAC associated fibroblasts, we observed that a subset of these neural genes were expressed at moderate levels in the healthy tissue (Figure 4A). This included neuronal genes *NEGR1, NRP1, NFIA*, and *SLIT2*. *EPHA3*, however, was specific to CAFs. As expected, and previously validated by others[23], *FAP* and *ACTA2* were higher in CAFs, while *PDGFRα, PDGFRβ, DPT*, and *CXCL12* were expressed in both populations. For further validation, we performed co-immunofluorescent staining of a donor pancreas tissue for PDGFRa, NRP1, and NEGR1 (Figure 4B,C and Supplementary Figure 2C, E). We observed the presence of these neural genes expressing fibroblasts near healthy pancreatic ducts (Supplementary Figure 2D, E), near pancreatic intraepithelial neoplasia (PanIN) identified in the healthy tissue (Figure 4B), and near healthy nerves (Figure 4C).The fibroblasts near the healthy nerves appeared adjacent to the epineurium, indicating they could be healthy fibroblasts of the epineurium.[24] These findings suggest that while elements of the NR-CAF signature are present in healthy pancreatic fibroblasts, the complete NR-CAF transcriptional program is confined to the malignant microenvironment and is further enriched following chemotherapy.

(NR+) CAFs exhibit axon guidance and Wnt gene expression programs and correlate with increased cognate receptor expression in tumor epithelial cells

To better understand the role that (NR+) CAFs may play in PDAC pathogenesis, we performed gene set enrichment analysis and found that (NR+) CAFs were significantly enriched for Wnt and Hedgehog signaling pathways, as well as axonal guidance, compared to (NR-) CAFs. (Figure 5A). We further investigated the Wnt pathway and observed that the (NR+) CAFs were enriched for non-canonical Wnt Ligand *Wnt5A*, and receptors *ROR2*, *FZD7*, as well as downstream targets such as *Myc* (Figure 5B). Neuronal signaling, specifically NRP1, has been previously associated to impact both hedgehog signaling and Wnt signaling targets[25]. Due to the prevalence of these pathways in cellular cross-talk, we extracted the tumor samples from our merged dataset and queried the expression of canonical ligand-receptor pairs enriched in individual cell populations. We observed that (NR+) CAFs expressed ligands involved in NRP1, NEGR1, and non-canonical Wnt signaling, as well as receptors for NRP1, and non-canonical Wnt signaling (Figure 5C). The cognate ligand-receptors for each of these pathways were most strongly expressed in epithelial cells, as well as endothelial cells and pericytes (Figure 5C). We further observed that the gene expression of a subset of these cognate ligand-receptor pairs were correlated between (NR+) CAFs and epithelial cells (Figure 5D). We validated the epithelial and tumor microenvironment expression of both NRP1 and SEMA3a through immunofluorescent expression of NRP1 in both tumor and stromal cells, as well as RNAscope expression of SEMA3a in both cell types (Figure 5E). While these interactions are inferred from gene expression data, it highlights the potential for a functional role of NR+ CAFs in the tumor microenvironment and indicates they may diverge in function from canonical CAFs due to exposure to chemotherapy and tumor microenvironment remodeling post-treatment.

(NR+) CAFs are enriched near regions of perineural invasion in both treatment-naïve and treated PDAC, whereas their presence in tumor areas distant from nerves is specifically elevated following chemotherapy.

As single cell RNA sequencing does not preserve spatial information, we performed co-immunofluorescent staining on treatment naïve and treated patient PDAC tissue to identify the spatial localization of (NR+) CAFs. Under guidance of a trained pathologist, we identified areas of tumor-nerve interactions, tumor glands in isolation, and nerves in isolation within each patient sample. Using αSMA as a fibroblast marker, we quantified the amount of NEGR1+ CAFs present in the stroma surrounding each of these structures. We observed that NEGR1+ CAFs were more abundant near nerves, particularly in areas of identified perineural invasion (Figure 6A, B, C). Furthermore, when we separated our patients into treatment categories, we did not see differences in the percentage (NR+) CAFs before and after treatment in areas of tumor-nerve interactions (Figure 6D), but we did see an enrichment post treatment in areas of tumor glands in isolation (Figure 6D, E). We also validated these findings with a second NR-CAF marker – NRP1 - and found similar results (Supplementary Figure 3A, B, C). Furthermore, when looking at distance from nerve structures, we saw that the percentage of (NR+) CAFs was highest within 200 um from tumor invaded nerves, whereas percentages of these CAFs maintained stable from distances of 0-300 um near tumor cells alone (Figure 6C). Nerve cells in the absence of any evidence of perineural invasion showed a slightly different distribution, with low levels of (NR+) CAFs immediately adjacent to the nerve, followed by an increase that correlated with distance that ultimately matched levels of (NR)+ CAFs near perineural invasion (Figure 6C). This was likely due to the fact that nerves in isolation in pancreatic tissue had limited stroma surrounding them as compared to areas with tumor cells present. Altogether, we found that NR-CAFs are enriched in areas of perineural invasion, irrespective of treatment status. In contrast, in areas of tumor non-adjacent to perineural invasion, (NR+) CAFs are enriched in post-treatment samples compared to treatment naive tumors. These findings indicate that the acquisition of the NR-CAF signature in fibroblasts may result from tumor–nerve interactions, or alternatively, may be promoted by the selective pressures of chemotherapy.

PDAC recurrence displays synchronous enrichment of neural genes in both CAFs, and tumor cells compared to the treatment naïve primary tumor.

Given the significant trends of NR-CAF enrichment in tumors with treatment, we sought to query the potential effect of these CAFs on the tumor cells themselves. Of unique interest to us was patient 1475, from whom we

obtained a third point for analysis in the setting of cancer recurrence. Patient 1475 received neoadjuvant treatment and chemoradiation followed by total pancreatectomy, with surgical pathology showing near complete response to treatment, reflected in our single cell sequencing sample which captured no tumor cells (Figure 7A, Supplementary Table 1A). However, 13 months post resection, this patient developed a para-aortic mass which was found to be a recurrence of their disease when biopsied (Figure 7A). We observed that the inferred copy number alterations in the recurrence had a high degree of concordance to the original mass, (Figure 7A), consistent with prior genomic work in this field.[26–31] We further queried the CAF population in this patient and observed that the myCAF population was heavily reduced post-chemotherapy and had lower expression in the recurrence as well. Both the iCAF population and NR+ CAF population were increased in the primary tumor site post-treatment (Figure 7C), but in the recurrence there was less iCAF gene expression. Notably, the NR+ CAF population was enriched immediately post-treatment and continued to be expressed at high levels within the recurrence, consistent with previous reports of neural-like malignant cells found in PDAC [5,32](Figure 7C). Looking closer at the epithelial changes in this patient, comparing the treatment-naïve timepoint to the recurrence timepoint, we observed that axonal guidance, Wnt signaling, and PI3K-Akt signaling were enriched in recurrent disease as compared to the treatment naïve primary tumor (Figure 7D). We specifically identified a variety of axonal guidance genes such as *NRG3, NTN1, SEMA4G, and NRP1* enriched in the recurrent tumor, as well as receptors for non-canonical Wnt5a (*ROR1, RYK, LRP6*) (Figure 7E). This shift towards a neural-like phenotype in cancer recurrence that mirrors the enrichment of neural genes in CAFs could be important in the context of cancer-nerve interactions. Furthermore, the (NR+) CAF population identified had increased Wnt-Signaling with specificity towards non-canonical Wnt ligand Wnt5a (Figure 5A, B), indicating potential crosstalk between tumor cells of the recurrence and (NR+) CAFs. In accordance with this, we further observed that areas of perineural invasion in patient tissues trended towards having higher levels of proliferating tumor cells compared to tumor areas non-adjacent to perineural invasion, regardless of treatment status (Figure 7F, G). Altogether, these data show that perineural invasion correlated with increased cell proliferation, and the localization of (NR+) CAFs to these areas, and their ability to signal with epithelial cells, especially in cancer recurrence, through Wnt and Axonal Guidance signaling, stations them to play a role in tumor cell proliferation and chemoresistance.

Discussion

In this study, we utilized a dataset generated by our lab that included five patient-matched samples before and after treatment and identified diverse tumor microenvironments through single-cell RNA sequencing and immunostaining validation. Utilizing multiple well-established bioinformatic pipelines and approaches[10,16,33], we investigated the heterogeneity of changes before and after treatment in epithelial cells, immune cells, and fibroblasts and profiled patient-specific and overall trends in transcriptomic changes induced by chemotherapy. While utilization of patient biospecimens studies offer the most faithful recapitulation of human disease, functionality is highly difficult to impute as studies are cross-sectional. However, the availability of matched samples in our dataset enabled us to discern authentic, patient-level effects of chemotherapy while accounting for the significant heterogeneity inherent to this disease. Here, we identified a near unanimous distinction in the cancer associated fibroblasts. A sub-group of CAFs were enriched for neural axonal guidance genes {*NEGR1, NRP1, NFIA, EPHA3, SLIT2, ROBO1, SEMA3A}*, termed (NR+) CAFs, after chemotherapy treatment, and had distinction features from myofibroblastic and inflammatory CAF signatures[20]. Our NR-CAF population abundance was high specifically in areas of perineural invasion regardless of treatment status but also elevated in tumor areas nonadjacent to nerves in treated tissues. Moreover, regions exhibiting perineural invasion demonstrated enhanced tumor cell proliferation. Coupled with the observation that neural gene expression in fibroblasts correlated with neural gene expression in tumor epithelial cells across samples, these findings suggest the presence of a neural signaling axis between specific tumor cells and cancer-associated fibroblasts (CAFs) that contributes to increased tumor cell chemoresistance and survival; and which is supported by the growing literature in the field.

PDAC has an especially high tropism for nerves, with perineural invasion and nerve hypertrophy being histopathological hallmarks of the disease.[9] Nerve hypertrophy and hypersensitivity has been identified as early as chronic pancreatic inflammation, preceding the initiation of any form of disease. After PDAC development, cancerous cells have been identified in mouse models within sensory nerve ganglia and along the spinal cord due to this high level of nerve involvement.[34] Neural crosstalk has previously been established to mediate

pancreatic pathogenesis as early as tumor initiation as well, and the ablation of sensory neurons of the pancreas has actually been found to inhibit PDAC tumorigenesis in mice.[34,35] This is further supported by findings that axonal guidance signaling molecules play a role in PDAC growth and invasion, and that tumor cells pseudo-synapse to nerves due to these secreted factors and guidance cues.[36]

We identified in our dataset that a portion of our NR-CAF signature genes were expressed in fibroblasts obtained from healthy donor pancreata, albeit at lower levels then chemotherapy-treated CAFs. CAFs have been identified previously to not only have various subtypes, but also to express differing neuronal genes indicating a high level of plasticity.[5,37–39] This is especially true of neuron-associated fibroblasts, such as those withing the epineurium that express high levels of axonal guidance genes, and which interact both with peripheral nerves and Schwan cells.[24] The expression of only a portion of our NR-CAF signature genes indicate that while neuronal genes are recapitulated in healthy fibroblasts, likely due to populations responsible for nerve engagement, activation of these fibroblasts to CAFs during a malignant switch likely increases the expression of the other neuronal genes. This switch could allow tumor cells to co-opt this pathway as a survival mechanism.

The (NR+) CAFs in our dataset enriched expression post-treatment in 4 out of 5 patients, and *in situ* this enrichment was only observed in areas of tumor cells alone. (NR+) CAFs were highly expressed near PNI regardless of treatment status but expanded into the overall tumor microenvironment following chemotherapy exposure. The presence of these neuronal markers, and expansion to all areas of tumor could be indicative of a stress-induced de-differentiation of the CAFs that is then hijacked by the tumor due to the prevalence of neural ligand-receptors with the ability to provide novel avenues of tumor-CAF crosstalk. For example, axonal guidance molecules identified in our NR-CAF signature such as *NRP1*, the cognate co-receptor for semaphorins, have been reported in pancreatic cancer previously in the context of cell invasion, perineural invasion, and tumor growth.[40–42] Semaphorin expression in tumor cells have been found to encourage differentiation of neuronal progenitors in the cancer stroma and establish the interface between nerves and cancer cells.[9,43–46] Neuropillins have also been found to engage with *VEGFβ* and *TGFβ*, which are key growth factors involved in PDAC tumor progression.[42] Further, overexpression of *NRP1* in pancreatic cancer cell lines can encourage MAPK signaling, which we saw enriched in the tumor epithelial cells of the recurrent tumor in patient 1475 (**Figure 7D**) and which can drive chemoresistance to gemcitabine and 5-Fluoroacil *in vitro.*[47] Other work has identified both neuronal gene expressing CAFs and tumor cells, indicated to be enriched post treatment in an unmatched study of patients pre-and-post-chemotherapy,[5] as well as a neuroendocrine subtype of tumor cells in PDAC[48] associated with chemoresistance and increased Myc expression. This finding was recapitulated in our data given increased Myc expression in our chemotherapy enriched (NR+) CAF population. These studies, in conjunction with our findings, further highlight the potential for neuronal signaling to drive resistance to cytotoxic therapies.

While our dataset has strength in its matched longitudinal samples, the dataset was limited in its small size (n=5), as well as the heterogeneity of treatment plan and disease progression across patients. Furthermore, through analysis of inferred copy number variations,[10] we discovered a limited number of tumor epithelial cells present in our dataset post-treatment. We did, however, have the opportunity to study a subset of tumor epithelial cells due to the presence of a recurrence. We observed that the recurrent tumor cells had highly expressed genes involved in axonal guidance, and many of which have reported in connection to biomarkers of perineural invasion in pancreatic cancer.[49] The findings of axonal guidance cues such as *NTN1, NTN4, NGEF, NRP1, SEMA4G, NEG3* was highly encouraging, given that the recurrence was local (as opposed to distant), and thus perineural invasion was the likely mechanism of tumor escape. Furthermore, the canonical receptors for non-canonical Wnt ligand Wnt5a (*ROR1, ROR2, RYK*) were highly expressed in the recurrence, as well as epithelial cells in the merged dataset. The high expression of these genes, and the high expression of Wnt ligand binding pairs in (NR+) CAFs indicates a role for interactions with epithelial cells that could drive tumor cell proliferation, perineural invasion, and cancer recurrence. Non-canonical Wnt signaling has been studied in the context of PDAC tumorigenesis, and this pathway, especially ROR2 expression, has been found to drive both the cellular identity of precancerous lesions in PDAC, as well as a more aggressive cancer type that is resistance to the inhibition of KRAS.[50] However, while these findings were highly interesting, the inclusion of only one patient leaves it underpowered to conclude any changes of statistical significance.

Overall, the presence of both an increase in an axonal guidance signature in tumor cells and a near unanimous trend of increased (NR+) CAFs post-treatment indicates the importance of axonal guidance and neuronal genes in pancreatic cancer. Furthermore, the spatial localization of neuronal CAFs near areas of perineural invasion in pancreatic cancer patients leads us to hypothesize a role for these CAFs in cancer-nerve crosstalk and the response of peripheral nerves to invasion and injury.[51,52] While the direct mechanism of this enrichment and functionality of these CAFs is beyond the scope of this work, their further study and characterization would be a boon to the burgeoning field of cancer neurobiology. The presence of these (NR+) CAFs and their enrichment opens up the question of whether treatment with chemotherapy may inadvertently lead to changes in the microenvironment that can promote perineural invasion of surviving tumor epithelial cells and lead to cancer recurrence, and if so, what treatment strategies can be utilized for prevention of such outcomes.

Methods

Sample Collection

Human subjects' research and sample collection was conducted in accordance with the ethical guidelines outlined in the Belmont Report with approval by the Institutional Review Board at the University of Michigan (Ann Arbor, MI; IRB HUM00025339). Medical charts were reviewed to assess potential study patients who specifically had resectable, borderline resectable or locally advanced disease. This was done because these were patients who had the potential for surgery or fiducial marker placement, allowing for collection of a post-chemotherapy timepoint (T2).Tumor tissue was collected via surgical resection or fine needle biopsy as described previously.[23,53] With respect to healthy donor pancreas tissues, acquisition of donor pancreata for research purposes was approved by the Gift of Life research review group.

Single-Cell RNA Sequencing

Newly acquired samples were processed as described previously[12,23,53] and single-cell cDNA libraries were prepared and sequenced at the University of Michigan Advanced Genomics Core using the 10x Genomics Platform. Samples were run using 28x151 bp of sequencing to a depth of 100,000 reads according to the manufacturer's protocol with either NovaSeq or NovaSeqXPlus (Illumina) to generate de-multiplexed Fastq files. Convert Conversion Software v3.9.3 or v4.0 (Illumina) was used to generate de-multiplexed Fastq files. All files were processed and realigned with Cell Ranger v7.1.0 and aligned to the GRC38 transcriptome. Pre-processing and analysis were done using R version v4.4.0, RStudio version v2025.5.999.999, and Seurat version v5.1.0.[33] Samples were merged, batch corrected, filtered, and normalized as previously done.[12,23,53] Variable genes were identified via FindVariableFeatures() and then principle component analysis was applied via RunPCA with the genes defined in the preceding step. Cell clusters were identified as described previously[12,23]. Gene signatures scores (myCAF, iCAF, and immune markers of activation and exhaustion) were obtained from literature and gene set scoring was calculated on each cellular cluster using AUCell() as described.[23,54] Copy number variations were inferred using Numbat(v1.4.2) and applied on all samples, this pipeline utilized both gene expression and germline heterozygous SNPs to generate the copy number variation probability for each cell.[10] Data from healthy normal pancreas samples were used as a reference.[23] We performed functional annotation using the Kyoto Encyclopedia of Genes and Genomes (KEGG) enrichment analysis applied through the clusterProfiler package (RRID:SCR_016884). Further analysis on larger dataset was done by merging our generated data with human single-cell RNA sequencing (scRNA-seq) data were previously published.[23] Differential cell–cell communication was done using CellChat.[16] Cell–cell communication was calculated between each cell-type pair using the manually curated interaction database (CellChatDB) on the merged dataset described above. Inferred ligand-receptor pairs were calculated for specific pathways of interest with emphasis on (NR+) and (NR-) CAFs as senders and receivers. Pseudobulk analysis was performed on each cell type as described previously.[23]

Immunofluorescence Assessment

Formalin-fixed, paraffin-embedded tissue sections were processed for immunofluorescence staining following rehydration and antibody incubation steps. Slides were baked at 60 °C for 2 hours, cooled to room temperature, and deparaffinized with two 5-minute washes in Histoclear (Cat# 64111-04). Slides were then rehydrated through two 5-minute washes in 100% ethanol, one 5-minute wash in 95% ethanol, and one 5-minute wash in 70% ethanol, followed by two 2-minute washes in running deionized water. Antigen retrieval was performed by immersing slides in preheated 1X citrate buffer (Cat# HK080-9K) and steamed for 20 minutes. Slides were cooled

to room temperature on ice for 15 minutes, washed twice for two minutes in deionized water, and then 5 minutes in 1X Phosphate Buffered Saline (PBS). A hydrophobic barrier was drawn around the tissue sections using an A-PAP pen. Slides were incubated for 60 minutes at room temperature in blocking buffer (1% bovine serum albumin, 0.3 M glycine, 10.0% goat serum, 0.1% Tween 20 in 1X PBS). Following blocking, slides were incubated overnight at 4 °C with 150 µL of the primary antibody diluted in blocking buffer. Primary antibodies used were NEGR1 (Abcam, Cat# ab96071, RRID: AB_10679337, Rabbit, 1:200), NRP1 (Abcam, Cat# ab16786, RRID: AB_2298830, Rabbit, 1:200), E-Cadherin (Cell Signaling Technology, Cat# 14472, RRID: AB_2728770, 1:300), Caspase 3 (Cell Signaling Technology, Cat# 9664, RRID: AB_2070042, Rabbit, 1:200) and MKI67 (Cell Signaling Technology, Cat# 12075, RRID: AB_2728830, Mouse, 1:200). The following day, slides were washed three times for five minutes each in 1X PBS and incubated for 1 hour at room temperature in the dark with fluorophore-conjugated secondary antibody diluted in blocking buffer. Secondaries used included Goat Anti-mouse AF488 (Cat# A-11001, 1:500, RRID:AB_2534069) and Goat Anti-Rabbit AF647 (Cat# A- 21245, 1:500, RRID:AB_2535813).Slides were then washed three times for five minutes in 1X PBS and incubated overnight in fluorophore conjugated primary antibody (Pan-Cytokeratin (PanCK) Alexa Fluor 570 (Fisher Scientific, Cat# 50-112-3641, Mouse, pre-conjugated, 1:800) and α-Smooth Muscle Actin (αSMA) Alexa Fluor 555 (Abcam, Cat# ab184675, RRID: AB_2832195, Rabbit, pre-conjugated, 1:800)) diluted in blocking buffer. The following day slides were washed three times for five minutes each in 1X PBS and counterstained with DAPI (1:10000 in 1X PBS, for 5 minutes at room temperature. After three additional five-minute PBS washes, slides were mounted with ProLong™ Diamond Antifade (Cat# P36934), cover slipped and allowed to dry overnight in the dark. Slides were stored at 4 °C until imaging. Slides were imaged on Nikon Ti2 Widefield microscope at 10X and on Leica Stellaris Confocal 5 at 40X with oil.

Immunofluorescence Assessment with Tyramide Signal Amplification

Slides were processed the same as immunofluorescent assessment (detailed above) but with modifications per Alexa Fluor 488 Tyramide SuperBoost Kit instructions (Cat# B40922). After antigen retrieval, slides were cooled to room temperature on ice for 15 minutes, washed twice for two minutes in deionized water. Slides were incubated for 15 minutes in humidified chamber with 3 drop of kit provided 3% hydrogen peroxide and then washed 3 times for 2 minutes each in 1X Phosphate Buffered Saline (PBS). Slides were then blocked for 30 minutes at room temperature with provided blocking buffer (Component A). A hydrophobic barrier was drawn around the tissue sections using an A-PAP pen. Primary antibody for signal amplification was diluted in 1X PBS (Anti-PDGFR alpha + PDGFR beta antibody [Y92] – C terminal, Abcam, CAT#: ab32570, Rabbit, 1:500, RRID:AB_777165) and incubated 4-degrees C overnight. The next day, slides were washed three times for five minutes each in 1X PBS and 2-3 drops of provided Poly-HRP conjugated secondary antibody was added two 60 minutes at room temperature. Slides were washed three times for two minutes each in 1X PBS. Tyramide working solution was prepared from provided reagents in kit (100X Tyramide stock solution (1:100), 100x H202 solution (1:100), 1X reaction buffer). 100 ul of the working solution was incubated on samples for 8 minutes in the dark. 100 ul of the provided working stop reagent (1:11 dilution in PBS) was added directly to slides and incubated for 5 minutes in the dark. Slides were washed three times for two minutes each in 1X PBS. Immunofluorescence assessment protocol was continued from this step starting at antigen retrieval step (described above) for remainder of antibodies.

RNA Scope

Patient tissue slides were baked and dewaxed following the immunofluorescence assessment protocol above, then incubated in 100% Ethanol for 1 minute two times, then slides are allowed to air dry for 10 min. 2-4 drops of RNAscope Hydrogen Peroxide (Cat# 322381) were added to each slide for 10 minutes at room temperature. Slides were washed in distilled H20 2X for 2 minutes each. Slides were submerged in hot 1X Co-detection target retrieval solution for 15 minutes (10X co-detection target retrieval solution, Cat# 323810). Slides were immediately transferred to 250 ml distilled water and washed two times for two minutes each. Slides were then washed in 1X PBS with 0.1% tween 20 (PBS-T) for two minutes. A hydrophobic barrier was drawn around the tissue sections using an A-PAP pen. The slides were then incubated in 200 mL of 10% neutral buffered formalin for 30 minutes at room temperature. During the incubation, the 50X RNAscope wash buffer reagent (Cat# 310091) was heated at 40 degrees for 10 minutes, then diluted to 1X with distilled water. RNAScope probes were warmed for 10 minutes at 40 degrees Celsius in an incubator and cooled to room temperature. The TSA Plus Cy-3 was reconstituted in the TSA diluent (Akoya Bioscience, Cat# NEL744001KT, 1:2000). After formalin incubation, the slides were washed again in PBS-T for 2 minutes 3 times. 4 drops of RNAscope protease plus (Cat# 322381) was added to each slide and was incubated in the oven for 13 minutes at 40 degrees C in a

humidified tray. Slides were washed for two minutes in distilled water twice. 4-6 drops of the appropriate probe mix (Hs- SEMA3A, CAT#416561) were added to entirely cover each slide and then incubated for 2 hours at 40 degrees C in a humidified chamber. Slides were washed in warmed RNAscope wash buffer for 2 minutes at room temperature, repeat this twice. 4 drops of RNAscope multiplex FL v2 AMP 1 (Cat# 323110) was added to each slide for 30 min at 40 degrees C in a humidified tray. Slides were washed in warmed RNAscope wash buffer for 2 minutes at room temperature. Repeated with RNAscope multiplex FL v2 AMP 2 (Cat# 323110), and RNAscope multiplex FL v2 AMP 3 (Cat# 323110). With AMP3, place it in oven for only 15 minutes and then wash for 2 minutes with RNAscope wash buffer twice at room temperature. 4 drops of RNAscope multiplex FL v2 HRP blocker (Cat# 323110) were added to each slide for 15 min at 40 degrees C in a humidified tray. Slides were washed in warmed RNAscope wash buffer for 2 minutes at room temperature. 4 drops of RNAscope multiplex FL v2 HRP-C1 (Cat# 323110) was added to each slide for 15 min at 40 degrees C in a humidified tray. Slides were washed in warmed RNAscope wash buffer for 2 minutes at room temperature. 150 ul diluted TSA-Cy3 was added to each slide and incubated 30 min at 40 degrees Celsius in a humidified tray. Slides were washed in warmed RNAscope wash buffer for 2 minutes at room temperature. 4 drops of RNAscope multiplex FL v2 HRP blocker (Cat# 323110) was added to each slide for 15 min at 40 degrees C in a humidified tray. Slides were washed in warmed RNAscope wash buffer for 2 minutes at room temperature. Co-detection antibody diluent was added to slides for 30 minutes to block slides at room temperature. Primary antibody (NRP1 Abcam, Cat# ab16786, RRID: AB_2298830, Rabbit, 1:200 and ECAD Cell Signaling Technology, Cat# 14472, RRID: AB_2728770, 1:300) was diluted in the co-detection antibody diluent and placed on slides in 4 degrees overnight. The next day, slides were washed twice in PBS-T, add secondary antibody, and DAPI as done in immunofluorescence assessment (above). Slides were mounted with ProLong™ Diamond Antifade (Cat# P36934), cover slipped and allowed to dry overnight in the dark. Slides were stored at 4 °C until imaged. Slides were imaged on Nikon Ti2 Widefield microscope at 10X and on Leica Stellaris Confocal 5 at 40X with oil.

Image Analysis and Quantification

Images were quantified using FIJI (v2.14.01) and Python scripts run in Jupyter Notebook (v3.13.7). Full 4-channel *.ome.tif* files were pulled into FIJI and split into single channel images. Regions of interest were chosen using pathologist marked hematoxylin and eosin slides and then copied over to the DAPI channel for each fluorescence image. These ROIs were saved in FIJI, and a macro was used to apply settings to all channels and multi crop into 10 single channel regions of interest per tissue. These cropped files were read into a python script that allowed users to identify structures of interest to be analyzed. These polygons were then imported, along with all cropped single channel files into Jupyter Notebook and each channel was masked individually and then double positive masks were created for all CAFs (DAPI+ASMA+), neural CAFs (DAPI+ASMA+NEGR1+ and DAPI+ASMA+NRP1+), and proliferating tumor cells (DAPI+PANCK+KI67+) and all tumor cells (DAPI+PANCK+). Percent neural CAFs and percent proliferating tumor cells were calculated as a percentage of total CAFs and total tumor cells. ROIs were marked as having tumor-nerve involvement – identified as areas where tumor cells and nerves were within 300 um of each other, or having just nerves in healthy stromal tissue, or tumor cells away from areas of nerve involvement. Percentages of each cell type were graphed with all ROIs merged or split by structure and/or treatment status of the patient. We stained n=11 treatment naïve and n=10 treated patient tissues, but due to poor tissue quality of some patients we quantified n=11 treatment naïve and n=6 treated patients. In the python script, double positive cells were calculated in outward radiuses starting from the border of the identified structure (either a nerve, or a path of tumor cells) at 50 um distances up to 300 um away from the structure border. For overall differences in structures and treatment, all radial bins were summed. Neural CAFs were also calculated as a function of distance from the structure and graphed in this way. Significance was calculated in GraphPad Prism 10 with a two-tailed student t-test between categories of interest. Proliferating tumor cells from each region of each patient were graphed against percent neural CAFs to identify correlations, this was also split by structure and by treatment status. Correlations were analyzed with linear regression.

Statistical Analysis

Statistical analysis were either performed with RStudio for single-cell RNA sequencing analysis utilizing a Wilcoxon rank sum test from the ggpubr package with stat_compare_means() or in GraphPad Prism 10 with a

two-tailed student t-test between groups of interest (paired t-test for individual patient analyses) or linear regression for correlative analyses.

Acknowledgements

We sincerely thank all patients and organ donors who have generously provided tissue for this research. We thank D. Postiff from the University of Michigan Tissue Procurement Core for procurement of surgical samples. We thank T. Tamsen, M. Hogan and J. Opp from the University of Michigan Advanced Genomics Core for their assistance with single cell RNA sequencing. We thank the University of Michigan Advanced Microscopy Core for assistance acquiring immunofluorescent images. We thank Hamadi Madhi for his assistance with single cell sequencing library preparation. We thank Christopher Strayhorn for histology services. We acknowledge the Rogel and Blondy Center for Pancreatic Cancer for its support of this study. Work in Carpenter Lab was supported by the Department of Veterans Affairs BLRD Career Development Award CDA IK2BX005875, the American College of Gastroenterology Career Development Award, the Research Scouts Award by the University of Michigan, and the Cancer Discovery Award by the University of Michigan Rogel Cancer Center. The funders had no role in study design, data collection and analysis, decision to publish or preparation of the manuscript. A.Z.H was supported by NIGMS GM150581. P.K. was supported by NIH/NIAID T32-AI007413 and NIH/NIGMS T32-GM113900.

References

1. Li, X., Liu, Z., Ye, Z., Gou, S. & Wang, C. Impact of age on survival of patients with pancreatic cancer after surgery: Analysis of SEER data. *Pancreatology* **18**, 133–138 (2018).

2. Halbrook, C. J., Lyssiotis, C. A., Pasca Di Magliano, M. & Maitra, A. Pancreatic cancer: Advances and challenges. *Cell* **186**, 1729–1754 (2023).

3. Beatty, G. L., Werba, G., Lyssiotis, C. A. & Simeone, D. M. The biological underpinnings of therapeutic resistance in pancreatic cancer. *Genes Dev.* **35**, 940–962 (2021).

4. Werba, G. *et al.* Single-cell RNA sequencing reveals the effects of chemotherapy on human pancreatic adenocarcinoma and its tumor microenvironment. *Nat Commun* **14**, 797 (2023).

5. Hwang, W. L. *et al.* Single-nucleus and spatial transcriptome profiling of pancreatic cancer identifies multicellular dynamics associated with neoadjuvant treatment. *Nat Genet* **54**, 1178–1191 (2022).

6. Zhou, X. *et al.* Persister cell phenotypes contribute to poor patient outcomes after neoadjuvant chemotherapy in PDAC. *Nat Cancer* **4**, 1362–1381 (2023).

7. Bapat, A. A., Hostetter, G., Von Hoff, D. D. & Han, H. Perineural invasion and associated pain in pancreatic cancer. *Nat Rev Cancer* **11**, 695–707 (2011).

8. Crippa, S. *et al.* Implications of Perineural Invasion on Disease Recurrence and Survival After Pancreatectomy for Pancreatic Head Ductal Adenocarcinoma. *Ann Surg* **276**, 378–385 (2022).

9. Jurcak, N. R. *et al.* Axon Guidance Molecules Promote Perineural Invasion and Metastasis of Orthotopic Pancreatic Tumors in Mice. *Gastroenterology* **157**, 838-850.e6 (2019).

10. Gao, T. *et al.* Haplotype-aware analysis of somatic copy number variations from single-cell transcriptomes. *Nat Biotechnol* **41**, 417–426 (2023).

11. Stromnes, I. M. *et al.* Targeted depletion of an MDSC subset unmasks pancreatic ductal adenocarcinoma to adaptive immunity. *Gut* **63**, 1769–1781 (2014).

12. Steele, N. G. *et al.* Multimodal mapping of the tumor and peripheral blood immune landscape in human pancreatic cancer. *Nat Cancer* **1**, 1097–1112 (2020).

13. Zheng, H., Li, Y., Zhao, Y. & Jiang, A. Single-cell and bulk RNA sequencing identifies T cell marker genes score to predict the prognosis of pancreatic ductal adenocarcinoma. *Sci Rep* **13**, 3684 (2023).

14. Freed-Pastor, W. A. *et al.* The CD155/TIGIT axis promotes and maintains immune evasion in neoantigen-expressing pancreatic cancer. *Cancer Cell* **39**, 1342-1360.e14 (2021).

15. Bockorny, B. *et al.* BL-8040, a CXCR4 antagonist, in combination with pembrolizumab and chemotherapy for pancreatic cancer: the COMBAT trial. *Nat Med* **26**, 878–885 (2020).

16. Jin, S., Plikus, M. V. & Nie, Q. CellChat for systematic analysis of cell-cell communication from single-cell and spatially resolved transcriptomics. Preprint at https://doi.org/10.1101/2023.11.05.565674 (2023).

17. Pei, G. *et al.* Spatial mapping of transcriptomic plasticity in metastatic pancreatic cancer. *Nature* **642**, 212–221 (2025).

18. Kemp, S. B. *et al.* Pancreatic cancer is marked by complement-high blood monocytes and tumor-associated macrophages. *Life Sci. Alliance* **4**, e202000935 (2021).

19. Lorestani, P. *et al.* The complex role of macrophages in pancreatic cancer tumor microenvironment: a review on cancer progression and potential therapeutic targets. *Discov Oncol* **15**, 369 (2024).

20. Öhlund, D. *et al.* Distinct populations of inflammatory fibroblasts and myofibroblasts in pancreatic cancer. *J Exp Med* **214**, 579–596 (2017).

21. Buechler, M. B. *et al.* Cross-tissue organization of the fibroblast lineage. *Nature* **593**, 575–579 (2021).

22. Krishnamurty, A. T. *et al.* LRRC15+ myofibroblasts dictate the stromal setpoint to suppress tumour immunity. *Nature* **611**, 148–154 (2022).

23. Carpenter, E. S. *et al.* Analysis of Donor Pancreata Defines the Transcriptomic Signature and Microenvironment of Early Neoplastic Lesions. *Cancer Discovery* **13**, 1324–1345 (2023).

24. Peng, K. *et al.* Magnetic separation of peripheral nerve-resident cells underscores key molecular features of human Schwann cells and fibroblasts: an immunochemical and transcriptomics approach. *Sci Rep* **10**, 18433 (2020).

25. Hillman, R. T. *et al.* Neuropilins are positive regulators of Hedgehog signal transduction. *Genes Dev* **25**, 2333–2346 (2011).

26. Moffitt, R. A. *et al.* Virtual microdissection identifies distinct tumor- and stroma-specific subtypes of pancreatic ductal adenocarcinoma. *Nat Genet* **47**, 1168–1178 (2015).

27. Chan-Seng-Yue, M. *et al.* Transcription phenotypes of pancreatic cancer are driven by genomic events during tumor evolution. *Nat Genet* **52**, 231–240 (2020).

28. Bailey, P. *et al.* Genomic analyses identify molecular subtypes of pancreatic cancer. *Nature* **531**, 47–52 (2016).

29. Boj, S. F. *et al.* Organoid Models of Human and Mouse Ductal Pancreatic Cancer. *Cell* **160**, 324–338 (2015).

30. Yachida, S. *et al.* Clinical Significance of the Genetic Landscape of Pancreatic Cancer and Implications for Identification of Potential Long-term Survivors. *Clinical Cancer Research* **18**, 6339–6347 (2012).

31. Sakamoto, H. *et al.* The Evolutionary Origins of Recurrent Pancreatic Cancer. *Cancer Discov* **10**, 792–805 (2020).

32. Biankin, A. V. *et al.* Pancreatic cancer genomes reveal aberrations in axon guidance pathway genes. *Nature* **491**, 399–405 (2012).

33. Hao, Y. *et al.* Integrated analysis of multimodal single-cell data. *Cell* **184**, 3573-3587.e29 (2021).

34. Stopczynski, R. E. *et al.* Neuroplastic Changes Occur Early in the Development of Pancreatic Ductal Adenocarcinoma. *Cancer Research* **74**, 1718–1727 (2014).

35. Saloman, J. L. *et al.* Ablation of sensory neurons in a genetic model of pancreatic ductal adenocarcinoma slows initiation and progression of cancer. *Proc. Natl. Acad. Sci. U.S.A.* **113**, 3078–3083 (2016).

36. Ren, L. *et al.* Sensory neurons drive pancreatic cancer progression through glutamatergic neuron-cancer pseudo-synapses. *Cancer Cell* S1535610825003952 (2025) doi:10.1016/j.ccell.2025.09.003.

37. Francescone, R. *et al.* Netrin G1 Promotes Pancreatic Tumorigenesis through Cancer-Associated Fibroblast-Driven Nutritional Support and Immunosuppression. *Cancer Discov* **11**, 446–479 (2021).

38. Grünwald, B. T. *et al.* Spatially confined sub-tumor microenvironments in pancreatic cancer. *Cell* **184**, 5577-5592.e18 (2021).

39. Sherman, M. H. & Di Magliano, M. P. Cancer-Associated Fibroblasts: Lessons from Pancreatic Cancer. *Annu. Rev. Cancer Biol.* **7**, 43–55 (2023).

40. Telley, L. *et al.* Dual Function of NRP1 in Axon Guidance and Subcellular Target Recognition in Cerebellum. *Neuron* **91**, 1276–1291 (2016).

41. Xin, Y. *et al.* Anti-Neuropilin-1 (MNRP1685A): Unexpected Pharmacokinetic Differences Across Species, from Preclinical Models to Humans. *Pharm Res* **29**, 2512–2521 (2012).

42. Matkar, P. N. *et al.* Jack of many trades: Multifaceted role of neuropilins in pancreatic cancer. *Cancer Med* **7**, 5036–5046 (2018).

43. Allen, J. K. *et al.* Sustained Adrenergic Signaling Promotes Intratumoral Innervation through BDNF Induction. *Cancer Research* **78**, 3233–3242 (2018).

44. Hoover, G. *et al.* Nerve-to-cancer transfer of mitochondria during cancer metastasis. *Nature* https://doi.org/10.1038/s41586-025-09176-8 (2025) doi:10.1038/s41586-025-09176-8.

45. Ding, Y. *et al.* Semaphorin 4F as a Critical Regulator of Neuroepithelial Interactions and a Biomarker of Aggressive Prostate Cancer. *Clinical Cancer Research* **19**, 6101–6111 (2013).

46. Wang, H. *et al.* Semaphorin4F is a potential biomarker for clinical progression and prognosis in gastric cancer. *Int J Clin Exp Pathol* **16**, 210–224 (2023).

47. Wey, J. S. *et al.* Overexpression of neuropilin-1 promotes constitutive MAPK signalling and chemoresistance in pancreatic cancer cells. *Br J Cancer* **93**, 233–241 (2005).

48. Farrell, A. S. *et al.* MYC regulates ductal-neuroendocrine lineage plasticity in pancreatic ductal adenocarcinoma associated with poor outcome and chemoresistance. *Nat Commun* **8**, 1728 (2017).

49. Liu, Q. *et al.* Perineural invasion-associated biomarkers for tumor development. *Biomedicine & Pharmacotherapy* **155**, 113691 (2022).

50. Benitz, S. *et al.* ROR2 Regulates Cellular Plasticity in Pancreatic Neoplasia and Adenocarcinoma. *Cancer Discovery* **14**, 2162–2182 (2024).

51. Hwang, W. L. *et al.* Integrating priorities at the intersection of cancer and neuroscience. *Cancer Cell* S1535610824003623 (2024) doi:10.1016/j.ccell.2024.09.014.

52. Winkler, F. *et al.* Cancer neuroscience: State of the field, emerging directions. *Cell* **186**, 1689–1707 (2023).

53. Carpenter, E. S. *et al.* KRT17High/CXCL8+ tumor cells display both classical and basal features and regulate myeloid infiltration in the pancreatic cancer microenvironment. *Clinical Cancer Research* https://doi.org/10.1158/1078-0432.CCR-23-1421 (2023) doi:10.1158/1078-0432.CCR-23-1421.

54. Wang, R. H. & Thakar, J. Comparative analysis of single-cell pathway scoring methods and a novel approach. *NAR Genomics and Bioinformatics* **6**, lqae124 (2024).

Figure 1) Sc-RNA Sequencing of five matched patients pre- and post-chemotherapy reveals a diverse tumor microenvironment with transcriptomic variability

A) Schematic of workflow to samples from either fine needle biopsies (FNB) or surgical resection.
B) Timeline of patient sample collection, neoadjuvant chemotherapy treatments, and overall survival (for participants deceased at time of data freeze) and progression-free survival (for patients currently being monitored at time of data freeze).
C) Hematoxylin and eosin (H&E) sections of representative biopsies and surgical resection samples for the resectable patients in the cohort. For each patient panel, H&E of fine needle biopsy on the left and the surgical resection on the right.
D) UMAP of single-cell RNA sequencing dataset generated from patient samples split by treatment naïve samples (left) and treated samples (right).
E) Dot plot showing genes used to identify cell populations
F) UMAP reduction of single-cell RNA sequencing dataset with cells inferred by to be 'normal' in red and cells inferred to be 'tumor' in blue through inferred copy number variation analysis.
G) Bar plot with cell frequencies of inferred 'normal' and 'tumor' epithelial cells in treatment-naïve and treated samples by copy number variation inference.

Figure 1

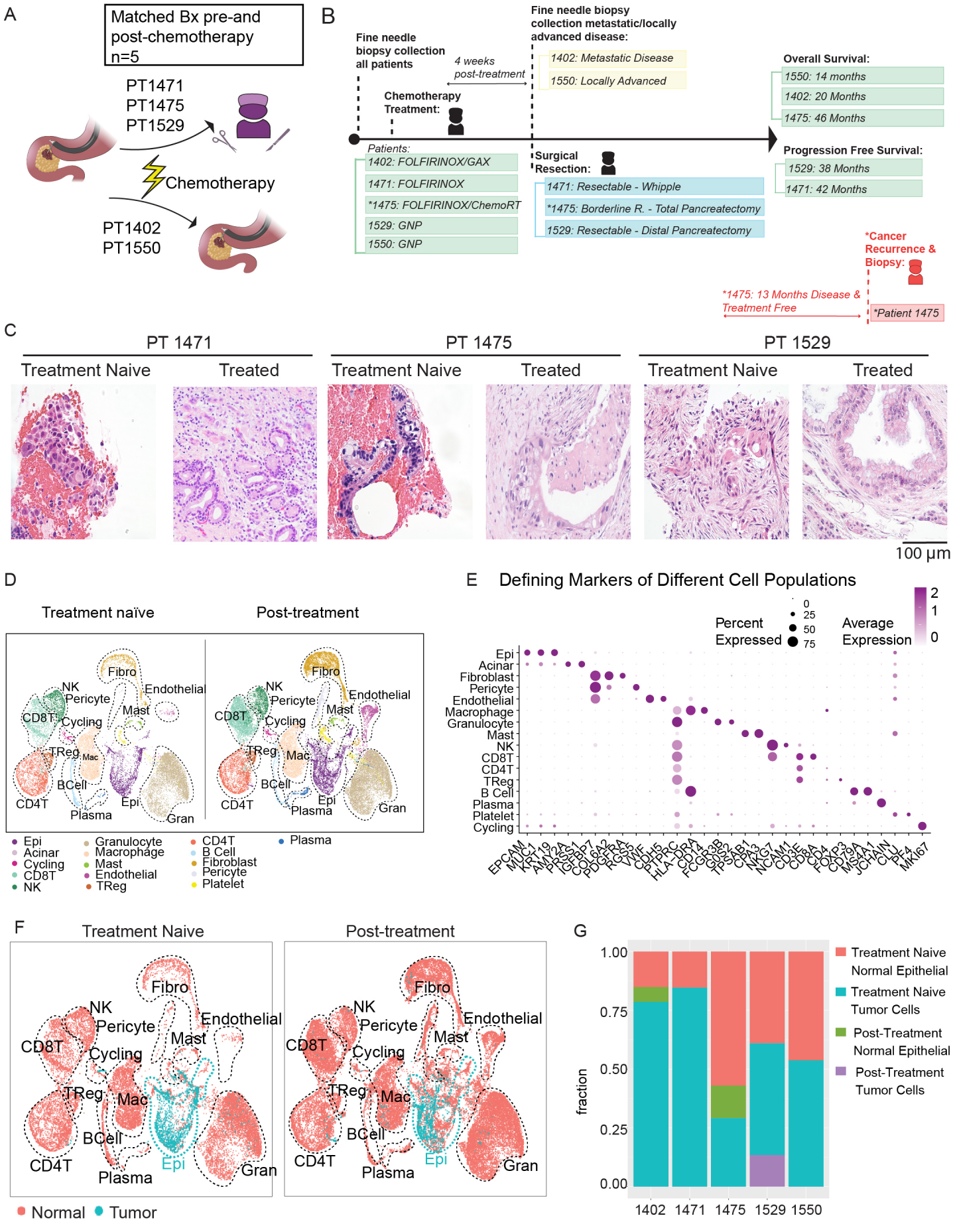
A
Matched Bx pre-and post-chemotherapy n=5
PT1471
PT1475
PT1529
Chemotherapy
PT1402
PT1550
B
Fine needle biopsy collection all patients
4 weeks post-treatment
Chemotherapy Treatment:
Fine needle biopsy collection metastatic/locally advanced disease:
1402: Metastatic Disease
1550: Locally Advanced
Patients:
1402: FOLFIRINOX/GAX
1471: FOLFIRINOX
*1475: FOLFIRINOX/ChemoRT
1529: GNP
1550: GNP
Surgical Resection:
1471: Resectable - Whipple
*1475: Borderline R. - Total Pancreatectomy
1529: Resectable - Distal Pancreatectomy
Overall Survival:
1550: 14 months
1402: 20 Months
1475: 46 Months
Progression Free Survival:
1529: 38 Months
1471: 42 Months
*Cancer Recurrence & Biopsy:
*1475: 13 Months Disease & Treatment Free
*Patient 1475
C
PT 1471
PT 1475
PT 1529
Treatment Naive
Treated
100 µm
D
Treatment naïve
Post-treatment
Fibro
NK
Pericyte
Endothelial
CD8T
Cycling
Mast
TReg
Mac
BCell
CD4T
Epi
Plasma
Gran
Epi
Acinar
Cycling
CD8T
NK
Granulocyte
Macrophage
Mast
Endothelial
TReg
CD4T
B Cell
Fibroblast
Pericyte
Platelet
Plasma
E
Defining Markers of Different Cell Populations
Percent Expressed
0
25
50
75
Average Expression
2
1
0
Epi
Acinar
Fibroblast
Pericyte
Endothelial
Macrophage
Granulocyte
Mast
NK
CD8T
CD4T
TReg
B Cell
Plasma
Platelet
Cycling
EPCAM
MUC1
KRT19
AMY2A
PRSS1
IGFBP7
COL6A2
PDGFRA
RGS5
VWF
CDH5
PTPRC
HLA-DRA
CD14
FCGR3B
COS2
TPSAB1
CPA3
NKG7
NCAM1
CD3E
CD8A
CD4
FOXP3
CD79A
MS4A1
JCHAIN
CLU
PECAM1
MKI67
F
Treatment Naive
Post-treatment
Fibro
NK
Pericyte
Endothelial
CD8T
Cycling
Mast
TReg
Mac
BCell
CD4T
Epi
Plasma
Gran
Normal
Tumor
G
1.00
0.75
0.50
0.25
0.00
fraction
1402
1471
1475
1529
1550
Treatment Naive Normal Epithelial
Treatment Naive Tumor Cells
Post-Treatment Normal Epithelial
Post-Treatment Tumor Cells

Figure 2. CXCR4 is unanimously enriched CD8+ T-cells post-treatment, with increased interactions between T-cells and cancer associated fibroblasts.

A) UMAP reduction of extracted T-cells and NK cells
B) Dot plot showing genes used to identify T-cell and NK sub-populations.
C) Before-and-after plots of immune-cell markers in each patient (CD8+ T-cells, top and CD4+ T-cells, bottom).
D) Feature plot showing gene expression of CXCR4 in all T-cells and NK cells in UMAP reduction of average gene expression scaled from 0 to 3 split by treatment naïve (top) and treated (bottom) T-cells of all patients.
E) Violin plots showing average CXCR4 gene expression in CD4 and CD8 T-cells and average CXCR4 and CXCL12 gene expression in cancer associated fibroblasts split by treatment status. Adjusted *P* value for significantly differentially expressed markers: *CXCR4 in T-cells < 2.2e-16 and CXCL12 in CAFs < 2.2e-16*.
F) Circle plots showing inferred ligand-receptor pairs between macrophages, T-cells, NK cells, and fibroblasts in treatment naïve samples from all patients (top) and treated samples from all patients (bottom).
G) UMAP of identified myeloid cell populations and cell frequency plot identifying fraction of cell subtypes in each population split across patient samples in treatment naïve and treated populations.
H) Dot plot of identifying genes in each myeloid cell population.

Figure 2

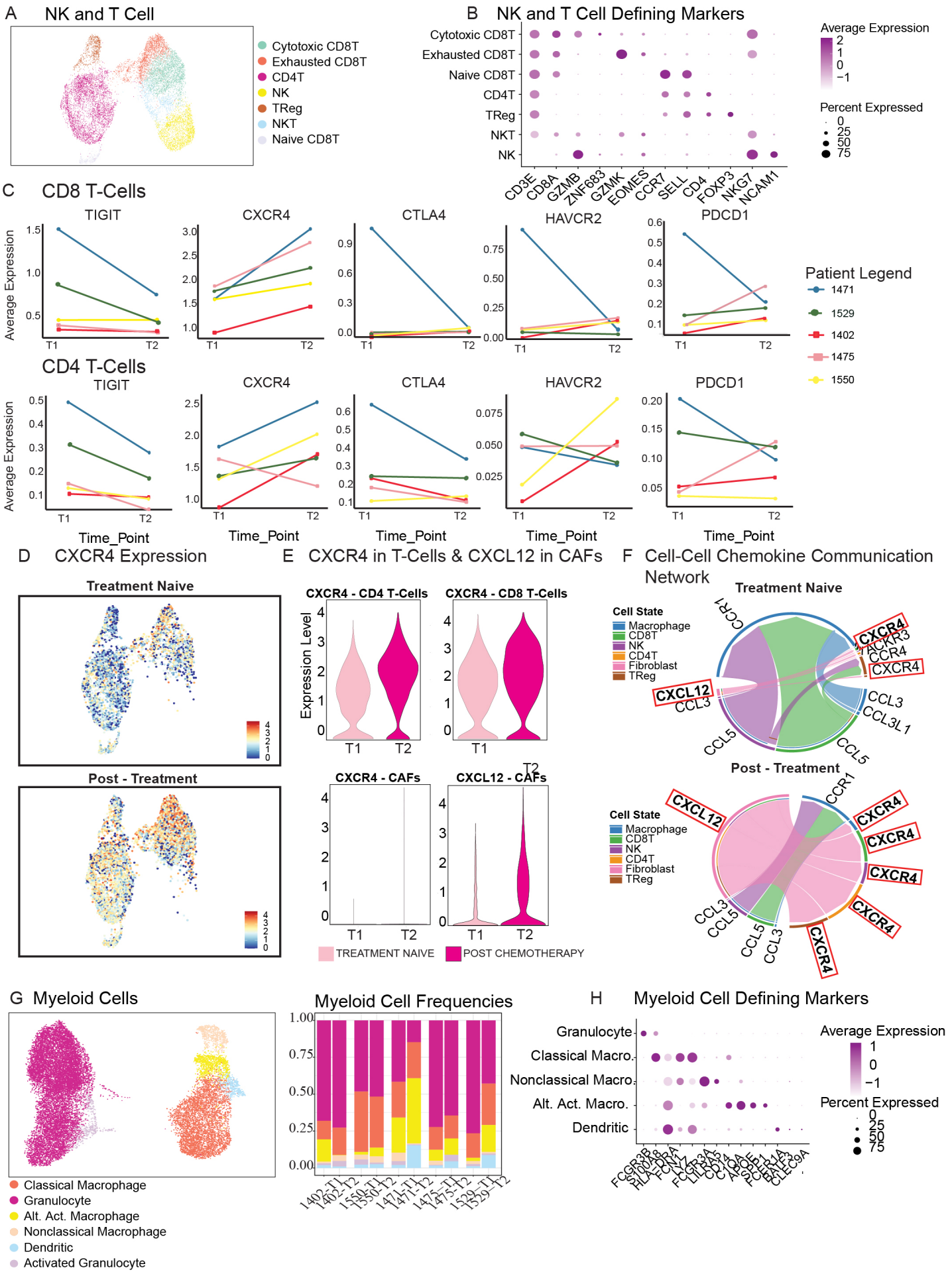
A NK and T Cell
Cytotoxic CD8T
Exhausted CD8T
CD4T
NK
TReg
NKT
Naive CD8T
B NK and T Cell Defining Markers
Cytotoxic CD8T
Exhausted CD8T
Naive CD8T
CD4T
TReg
NKT
NK
CD3E
CD8A
GZMB
ZNF683
GZMK
EOMES
CCR7
SELL
CD4
FOXP3
NKG7
NCAM1
Average Expression
Percent Expressed
C CD8 T-Cells
TIGIT
CXCR4
CTLA4
HAVCR2
PDCD1
Average Expression
T1
T2
Patient Legend
1471
1529
1402
1475
1550
CD4 T-Cells
Time_Point
D CXCR4 Expression
Treatment Naive
Post - Treatment
E CXCR4 in T-Cells & CXCL12 in CAFs
CXCR4 - CD4 T-Cells
CXCR4 - CD8 T-Cells
CXCR4 - CAFs
CXCL12 - CAFs
Expression Level
TREATMENT NAIVE
POST CHEMOTHERAPY
F Cell-Cell Chemokine Communication Network
Treatment Naive
Post - Treatment
Cell State
Macrophage
CD8T
NK
CD4T
Fibroblast
TReg
CCR1
CXCR4
ACKR3
CCR4
CXCL12
CCL3
CCL3L1
CCL5
G Myeloid Cells
Classical Macrophage
Granulocyte
Alt. Act. Macrophage
Nonclassical Macrophage
Dendritic
Activated Granulocyte
Myeloid Cell Frequencies
H Myeloid Cell Defining Markers
Granulocyte
Classical Macro.
Nonclassical Macro.
Alt. Act. Macro.
Dendritic
Average Expression
Percent Expressed

Figure 3. An 'axonal guidance' gene signature is enriched in a sub-population of CAFs following treatment..

A) UMAP reduction of extracted fibroblasts.
B) Histogram showing cell frequencies for Fibro1, Fibro2, and Fibro3, split by treatment status.
C) Dot plot showing top expressed genes in Fibro1, Fibro2, and Fibro3 populations.
D) Feature plot of fibroblast UMAP reduction showing average gene expression of *CXCL12, ACTA2* (left) and top expressed genes in Fibro3 (right).
E) Feature plot genes representative of AUCell gene signature scoring of myofibroblasts (top left), inflammatory fibroblasts (bottom left), and antigen presenting fibroblasts (top right), and UMAP reduction of fibroblasts with AUCell scoring of our NR-CAF gene signature (*NEGR1, NRP1, NFIA, ROBO1, SLIT2, SEMA3A, NFIA, EPHA3*) (bottom right)
F) Violin plots of average expression of NR-CAF and common fibroblast genes split by patient and colored by treatment status.
G) Heatmap of signature scores of NR-CAF gene signature, myofibroblastic gene signature, and inflammatory fibroblast gene signature split by patient ID and treatment status (T1 – treatment naïve and T2 – treated) (right)
H) UMAP reduction of merged dataset containing published dataset of 16 treatment naïve PDAC samples and our dataset of matched 5 treatment naïve PDAC samples and 5 treated PDAC samples with individual cell clusters marked, and (NR+) CAFs highlighted in pink.
I) Average gene expression of myofibroblastic genes (left), inflammatory fibroblast genes (middle), and axonal guidance (NR+) CAF genes (right) mapped to fibroblasts in merged dataset.
J) Violin plots of NR-CAF genes and *ACTA2* in treatment naïve PDAC samples (T1) and treated PDAC samples (T2) in the merged dataset. Adjusted *P* value for significantly differentially expressed markers: *NRP1 <4.9e-08, NEGR1 <2.2e-16, NFIA <2.2e-16, SLIT2 <2.2e-16, EPHA3 <2.2e-16, ACTA2 <2.2e16.*

Figure 3

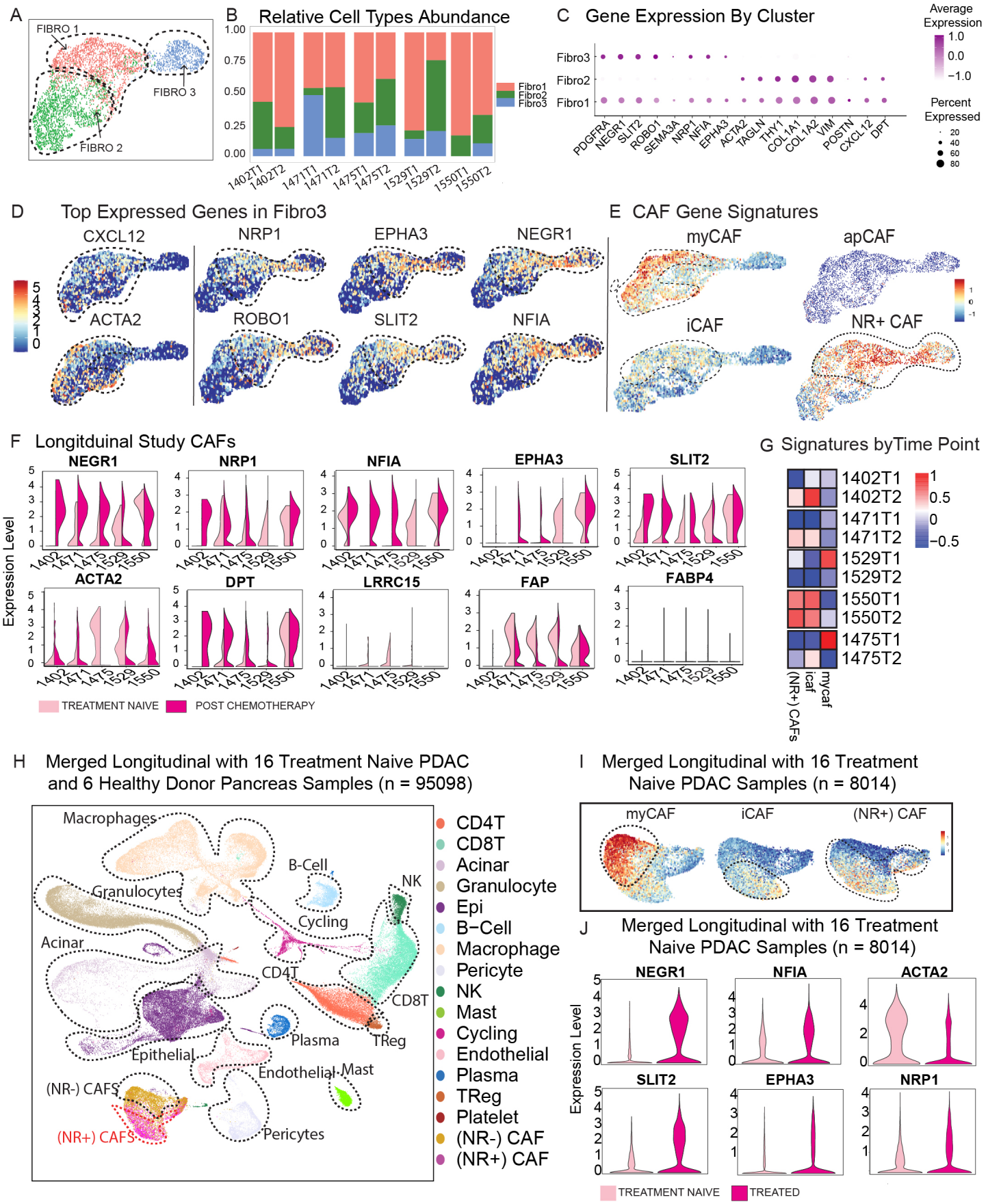
A
FIBRO 1
FIBRO 3
FIBRO 2
B Relative Cell Types Abundance
Fibro1
Fibro2
Fibro3
1402T1 1402T2 1471T1 1471T2 1475T1 1475T2 1529T1 1529T2 1550T1 1550T2
C Gene Expression By Cluster
Average Expression
Percent Expressed
Fibro3
Fibro2
Fibro1
PDGFRA NEGR1 SLIT2 ROBO1 SEMA3A NRP1 NFIA EPHA3 ACTA2 TAGLN THY1 COL1A1 COL1A2 VIM POSTN CXCL12 DPT
D Top Expressed Genes in Fibro3
CXCL12
NRP1
EPHA3
NEGR1
ACTA2
ROBO1
SLIT2
NFIA
E CAF Gene Signatures
myCAF
apCAF
iCAF
NR+ CAF
F Longitduinal Study CAFs
NEGR1
NRP1
NFIA
EPHA3
SLIT2
ACTA2
DPT
LRRC15
FAP
FABP4
Expression Level
1402 1471 1475 1529 1550
TREATMENT NAIVE
POST CHEMOTHERAPY
G Signatures byTime Point
1402T1
1402T2
1471T1
1471T2
1529T1
1529T2
1550T1
1550T2
1475T1
1475T2
(NR+) CAFs
icaf
mycaf
H Merged Longitudinal with 16 Treatment Naive PDAC and 6 Healthy Donor Pancreas Samples (n = 95098)
Macrophages
B-Cell
NK
Granulocytes
Cycling
Acinar
CD4T
CD8T
Plasma
TReg
Epithelial
Endothelial
Mast
(NR-) CAFS
(NR+) CAFS
Pericytes
CD4T
CD8T
Acinar
Granulocyte
Epi
B−Cell
Macrophage
Pericyte
NK
Mast
Cycling
Endothelial
Plasma
TReg
Platelet
(NR-) CAF
(NR+) CAF
I Merged Longitudinal with 16 Treatment Naive PDAC Samples (n = 8014)
myCAF
iCAF
(NR+) CAF
J Merged Longitudinal with 16 Treatment Naive PDAC Samples (n = 8014)
NEGR1
NFIA
ACTA2
SLIT2
EPHA3
NRP1
Expression Level
TREATMENT NAIVE
TREATED

Figure 4. The NR+CAF signature is partially recapitulated in the absence of malignancy

A) Violin plots of CAF markers and NR-CAF genes comparing healthy fibroblasts from healthy donor pancreata and PDAC samples. Adjusted *P* value for differentially expressed genes: *NRP1 0.07, NEGR1 0.00062, DPT 1.8e-07, NFIA <2.2e-16, FAP <2.2e-16, EPHA3 <2.2e-16, SLIT2 <2.2e-16, ACTA2 <2.2e-16, CXCL12 <2.2e-16, PDGFRA <2.2e-16, PDGFRB <2.2e-16.*
B) PanIN identified in healthy pancreas stained for DAPI (blue), PDGFRα (green), PANCK (white), and NRP1 (red).
C) Tissue resident nerve in healthy pancreas stained for DAPI (blue), PDGFRα (green), PANCK (white), and NRP1 (red).

Figure 4

A Merged Longitudinal Dataset with 16 Treatment Naive PDAC and 6 Healthy Donor Pancreas Samples (n=10211)

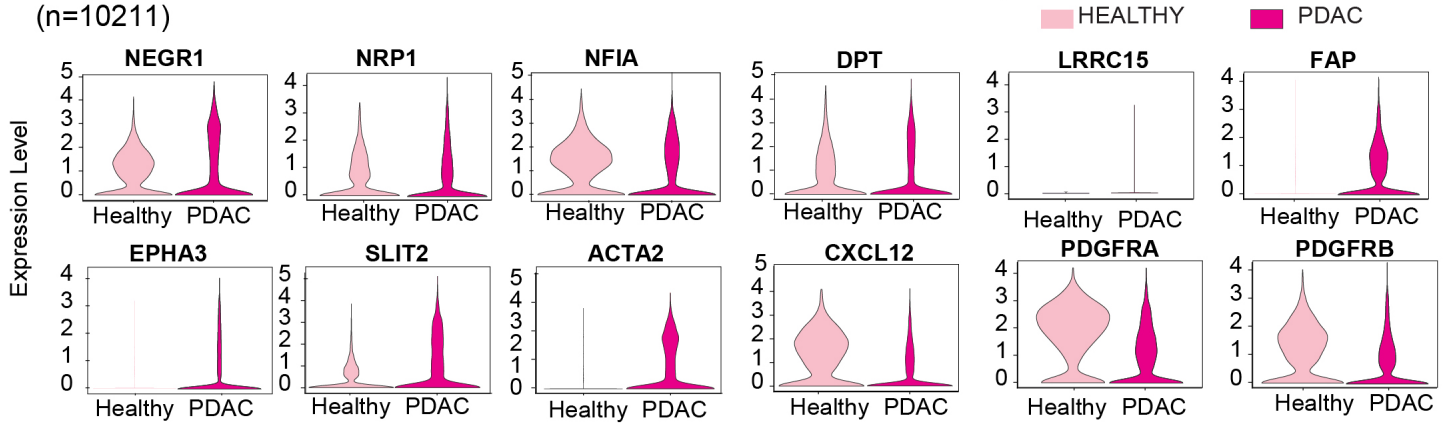

B PanIN from Healthy Donor Pancreata

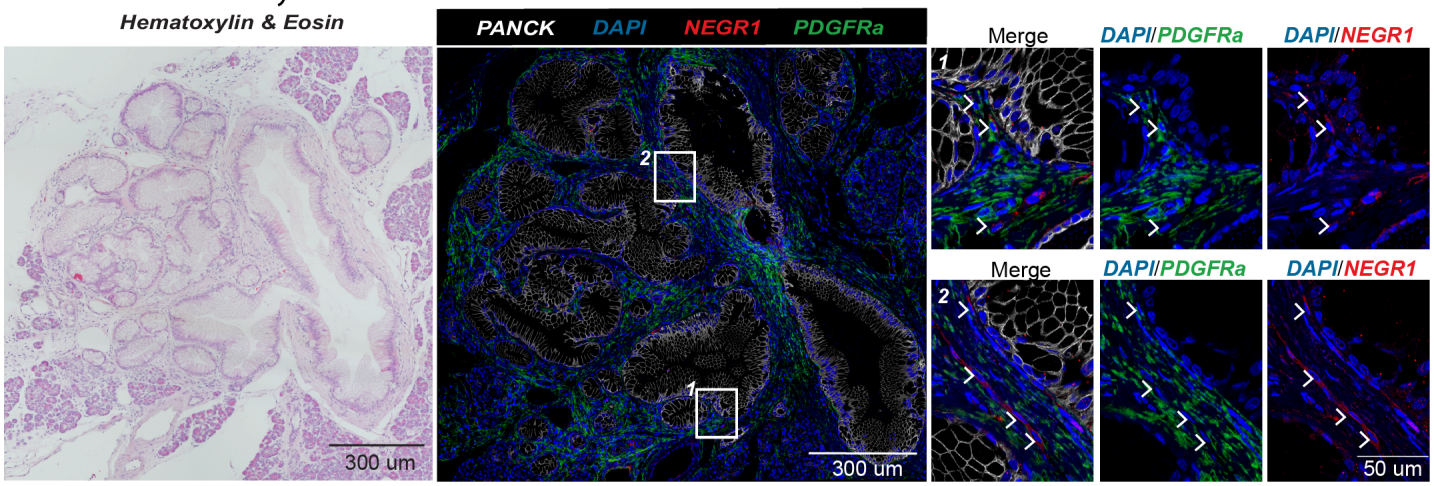

C Nerve from Healthy Donor Pancreata

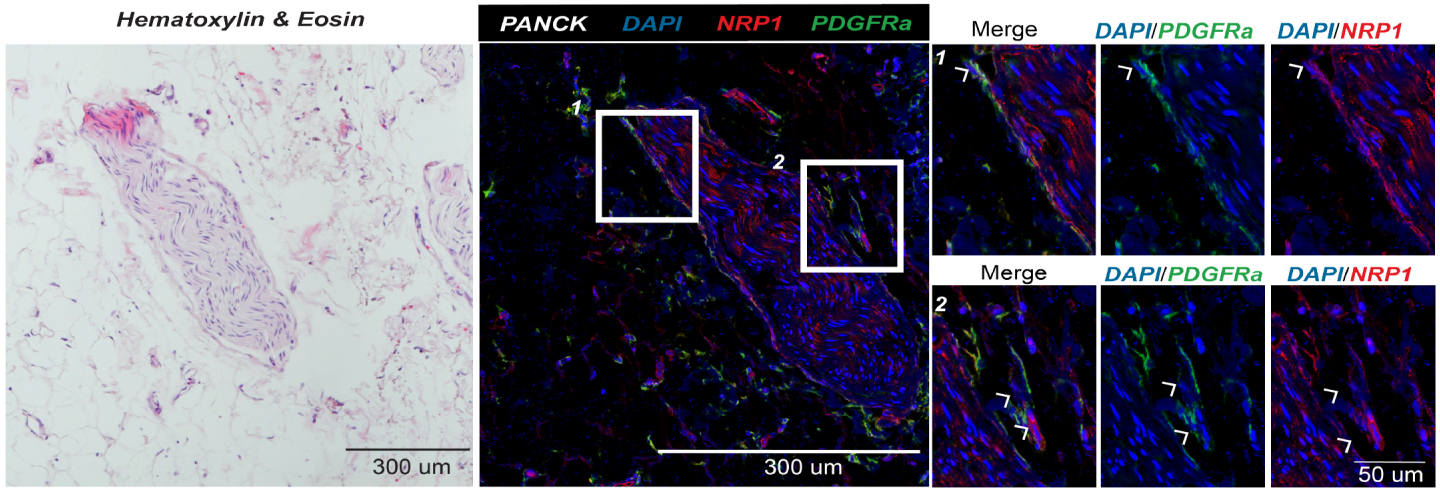

Figure 5. (NR+) CAFs exhibit axon guidance and Wnt gene expression programs and correlate with increased cognate receptor expression in tumor epithelial cells

A) Bar plot showing enriched pathways from the KEGG database comparing (NR+) CAFs to (NR-) CAFs, pathways of interest are highlighted in red.
B) Violin plot of top differentially expressed genes involved in Wnt signaling in (NR-) and (NR+) CAFs. Adjusted *P* Value for significantly differentially expressed genes: *WNT5A <2.9e-6, SFRP1 <2.9e-6, MYC <2.2e-16, ROR2 <2.2e-16, PRICKLE1 <2.2e-16, FZD7 <2.2e-16, PLCB4 <2.2e-16, LRP6 <2.2e-16* .
C) Dot plot of ligand-receptor pairs involved in NRP1, NEGR1, and non-canonical Wnt signaling in all cell subtypes - CAF (cancer associated fibroblast), Endo. (Endothelial cells), Peri. (Pericyte), Gran. (granulocyte), Epi. (epithelial)
D) Correlation matrix between ligand-receptor pairs expressed in either (NR+) CAFs or Epithelial cells. X-axis contains genes expressed in (NR+) CAFs and y-axis contains genes expressed in epithelial cells. Each cell displays the degree of correlation between genes expressed in each population. E, Immunofluorescence staining for DAPI (blue), E-Cadherin (white) and NRP1(red) with RNAscope for SEMA3A (green) in PDAC tumor area (left). White carrots indicate areas SEMA3A+NRP1+ cells at higher magnification (right).

Figure 5

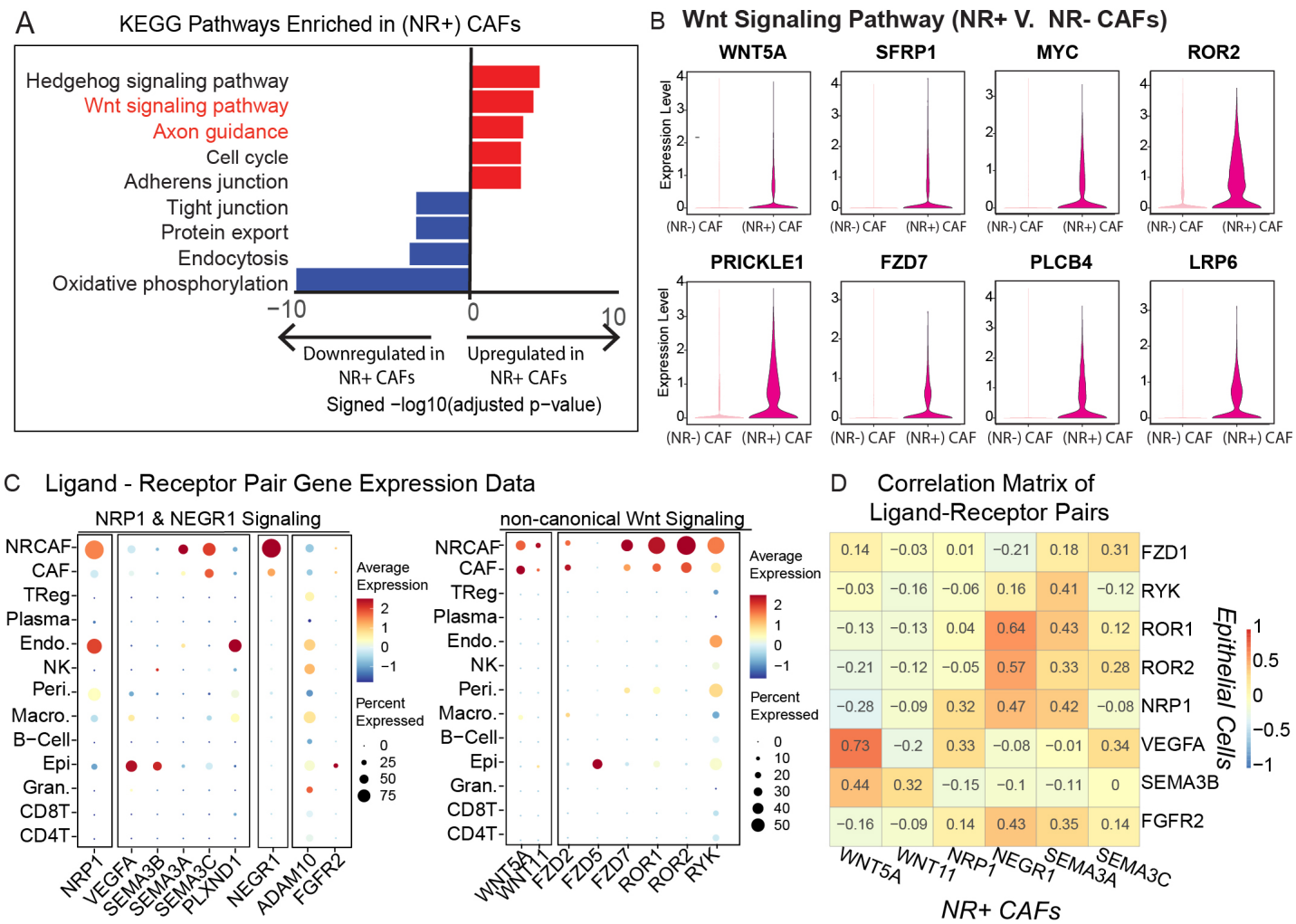
A
KEGG Pathways Enriched in (NR+) CAFs
Hedgehog signaling pathway
Wnt signaling pathway
Axon guidance
Cell cycle
Adherens junction
Tight junction
Protein export
Endocytosis
Oxidative phosphorylation
−10
0
10
Downregulated in NR+ CAFs
Upregulated in NR+ CAFs
Signed −log10(adjusted p−value)
B Wnt Signaling Pathway (NR+ V. NR- CAFs)
WNT5A
SFRP1
MYC
ROR2
PRICKLE1
FZD7
PLCB4
LRP6
Expression Level
(NR-) CAF
(NR+) CAF
C Ligand - Receptor Pair Gene Expression Data
NRP1 & NEGR1 Signaling
non-canonical Wnt Signaling
NRCAF
CAF
TReg
Plasma
Endo.
NK
Peri.
Macro.
B−Cell
Epi
Gran.
CD8T
CD4T
NRP1
VEGFA
SEMA3B
SEMA3A
SEMA3C
PLXND1
NEGR1
ADAM10
FGFR2
WNT5A
WNT11
FZD2
FZD5
FZD7
ROR1
ROR2
RYK
Average Expression
Percent Expressed
D Correlation Matrix of Ligand-Receptor Pairs
FZD1 0.14 −0.03 0.01 −0.21 0.18 0.31
RYK −0.03 −0.16 −0.06 0.16 0.41 −0.12
ROR1 −0.13 −0.13 0.04 0.64 0.43 0.12
ROR2 −0.21 −0.12 −0.05 0.57 0.33 0.28
NRP1 −0.28 −0.09 0.32 0.47 0.42 −0.08
VEGFA 0.73 −0.2 0.33 −0.08 −0.01 0.34
SEMA3B 0.44 0.32 −0.15 −0.1 −0.11 0
FGFR2 −0.16 −0.09 0.14 0.43 0.35 0.14
WNT5A
WNT11
NRP1
NEGR1
SEMA3A
SEMA3C
NR+ CAFs
Epithelial Cells
E Treatment Naive Tumor Tissue (patient 55818)
ECAD
DAPI
NRP1
SEMA3A
300 um
Merge
DAPI/SEMA3a
DAPI/NRP1
50 um

Figure 6. (NR+) CAFs are enriched near regions of perineural invasion in both treatment-naïve and treated PDAC, whereas their presence in tumor areas distant from nerves is specifically elevated following chemotherapy.

A) Hematoxylin and eosin staining of treatment naïve patient tissue (patient 1926) (left), and immunofluorescence staining of serial section from same patient tissue with DAPI, aSMA (green), PANCK (white), and NEGR1 (red) in an area marked as perineural invasion (middle). White arrows denote NEGR1+αSMA+ CAFs at higher magnification (right).
B) B, Hematoxylin and eosin staining of treatment naïve patient tissue (patient 1926) (left), and immunofluorescence staining of serial section from patient with DAPI, aSMA (green), PANCK (white), and NEGR1 (red) in tumor tissue non-adjacent to perineural invasion. White arrows denote NEGR1+αSMA+ CAFs and higher magnification (right).
C) Bar plot of percentage of (NR+) CAFs in regions of perineural invasion, tumor nonadjacent to perineural invasion, and nerve alone from each patient (N=17) with N=10 random regions of interest chosen for each patient. Spatial distribution plot showing percentage of (NR+) CAFs out of total CAFs in each structure at distance bin of 50 um intervals (right). Adjusted P value for %NR CAFs in areas of perineural invasion versus areas of tumor cells alone: *<0.0001*.
D) D, Bar plot of percentage of (NR+) CAFs in treatment naïve patients (N=11) and treated patients (N=6) with all structures included (left), only areas of perineural invasion (middle), and only areas of tumor non-adjacent to perineural invasion(right). Adjusted *P* values for treatment naïve versus treated patients: in tumor cells alone *0.0416*, all structures combined *0.1258*, and perineural invasion only *0.7671*.
E) Hematoxylin and eosin staining of treated patient tissue (patient 191999) (left), and immunofluorescence staining of serial section from same patient tissue with DAPI (blue), αSMA (green), PANCK (white), and NEGR1 (red) in an area marked as tumor only (middle). White arrows denote NEGR1+αSMA+ CAFs at higher magnification (right).

Figure 6

A Perieural Invasion (Treatment Naive) (Patient 1926)

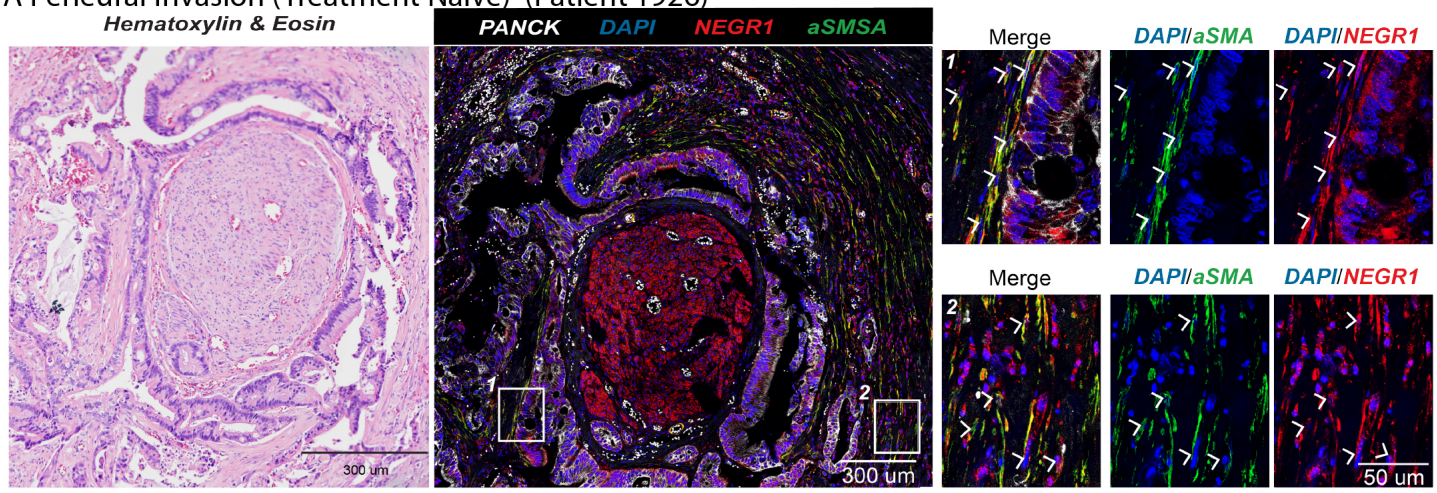

B Tumor (No Nerve, Treatment Naive) (Patient 1926)

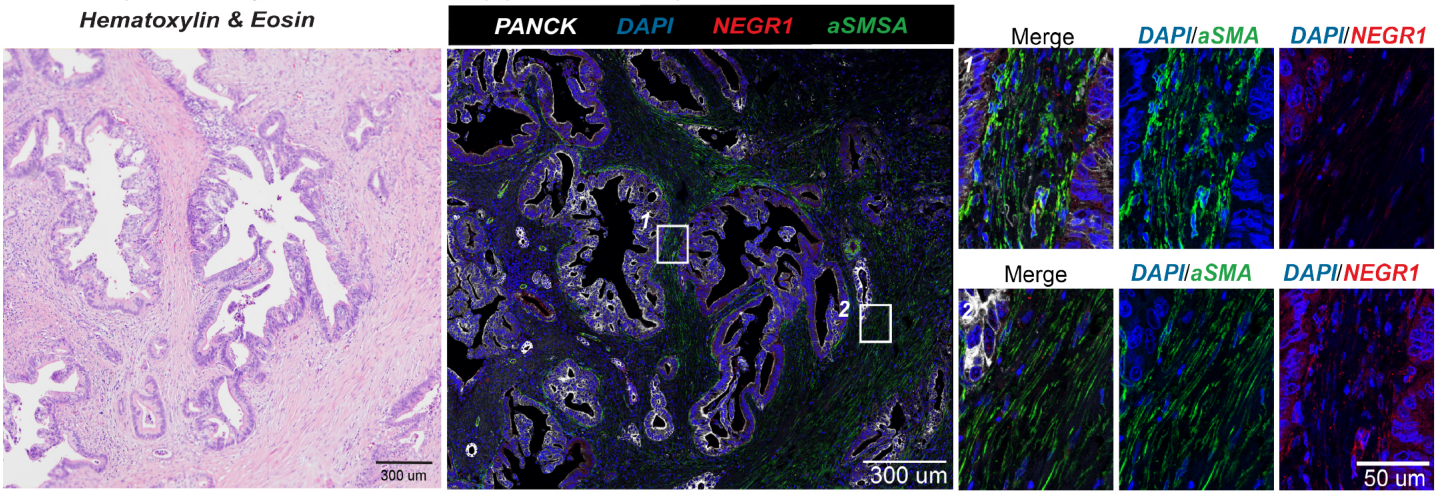

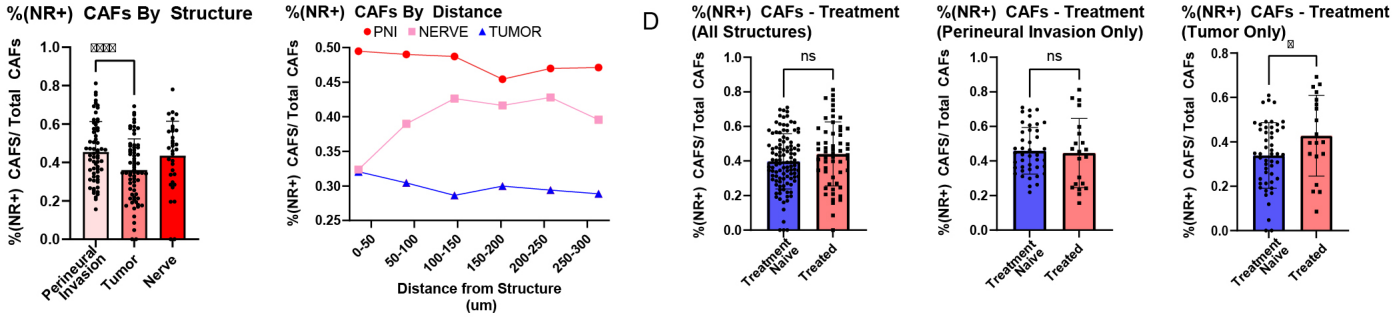

E Tumor (No Nerve, Treated) (Patient 19199)

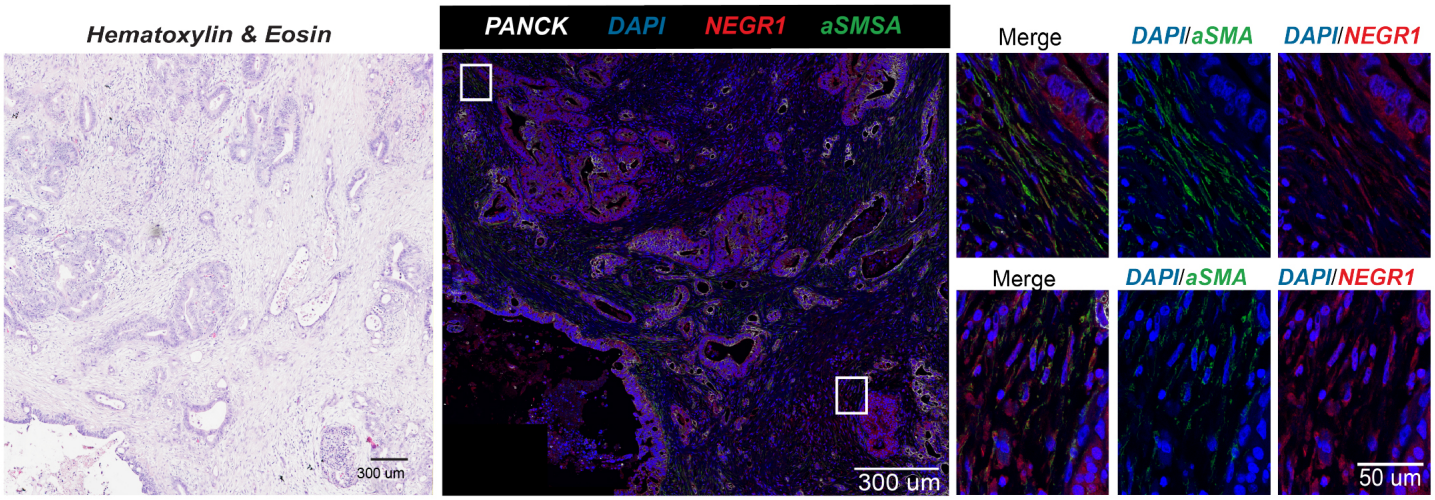

Figure 7. PDAC recurrence displays synchronous enrichment of neural genes in both CAFs and tumor cells compared to the treatment naïve primary tumor.

A) Timeline showing patient 1475 FNB, neoadjuvant therapy, surgical resection, and identification of recurrent disease (top). Computed Tomography scan of patient 1475 at time of diagnosis (left), post-surgery (middle), and at time of discovered cancer recurrence (right) tumor mass denoted by yellow arrows. Bottom: Heatmap of inferred copy number variation analysis of treatment naïve FNB and recurrence
B) Bar plot comparing cell type frequencies of patient 1475 specifically split between treatment naïve FNB, surgical sample post-therapy at time of resection, and recurrence biopsy.
C) Heatmap of average axonal-guidance gene signature expression split by treatment status in patient-1475 (T1 – treatment naïve, T2 – treated, T3 - recurrence).
D) Normalized enrichment score, of KEGG pathways comparing recurrence sample to treatment naïve tumor cells.
E) Top differentially expressed genes between tumor epithelial cells of patient 1475 treatment naïve FNB (left) and patient 1475 recurrence biopsy (right).
F) Co-immunofluorescence of area of perineural invasion and tumor nonadjacent to perineural invasion from patient 1926 tissue stained for DAPI (blue), a-SMA (green), PANCK (white), and MKI67 (red)
G) Quantification of average %KI67+PANCK+/Total PANCK+ cells in areas of PNI and areas of tumor alone, where each line represents one patient (paired t-test $P=0.07$).

Figure 7

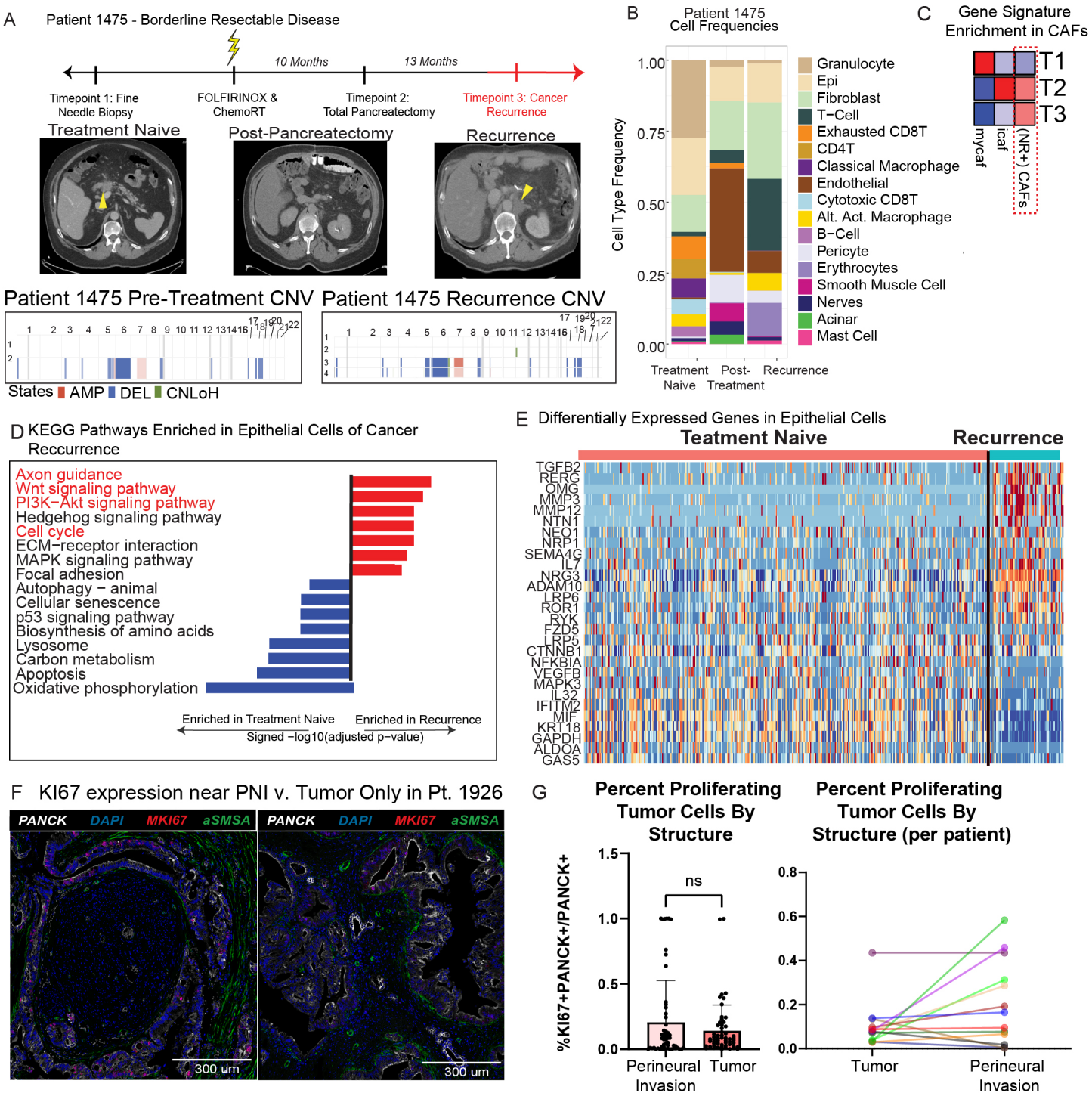
A
Patient 1475 - Borderline Resectable Disease
10 Months
13 Months
Timepoint 1: Fine Needle Biopsy
FOLFIRINOX & ChemoRT
Timepoint 2: Total Pancreatectomy
Timepoint 3: Cancer Recurrence
Treatment Naive
Post-Pancreatectomy
Recurrence
Patient 1475 Pre-Treatment CNV
Patient 1475 Recurrence CNV
States AMP DEL CNLoH
B
Patient 1475 Cell Frequencies
Cell Type Frequency
Treatment Naive
Post-Treatment
Recurrence
Granulocyte
Epi
Fibroblast
T−Cell
Exhausted CD8T
CD4T
Classical Macrophage
Endothelial
Cytotoxic CD8T
Alt. Act. Macrophage
B−Cell
Pericyte
Erythrocytes
Smooth Muscle Cell
Nerves
Acinar
Mast Cell
C
Gene Signature Enrichment in CAFs
T1
T2
T3
mycaf
icaf
(NR+) CAFs
D KEGG Pathways Enriched in Epithelial Cells of Cancer Reccurrence
Axon guidance
Wnt signaling pathway
PI3K−Akt signaling pathway
Hedgehog signaling pathway
Cell cycle
ECM−receptor interaction
MAPK signaling pathway
Focal adhesion
Autophagy − animal
Cellular senescence
p53 signaling pathway
Biosynthesis of amino acids
Lysosome
Carbon metabolism
Apoptosis
Oxidative phosphorylation
Enriched in Treatment Naive
Enriched in Recurrence
Signed −log10(adjusted p−value)
E Differentially Expressed Genes in Epithelial Cells
Teatment Naive
Recurrence
TGFB2
RERG
OMG
MMP3
MMP12
NTN1
NEO1
NRP1
SEMA4G
IL7
NRG3
ADAM10
LRP6
ROR1
RYK
FZD5
LRP5
CTNNB1
NFKBIA
VEGFB
MAPK3
IL32
IFITM2
MIF
KRT18
GAPDH
ALDOA
GAS5
F KI67 expression near PNI v. Tumor Only in Pt. 1926
PANCK DAPI MKI67 aSMSA
PANCK DAPI MKI67 aSMSA
300 um
300 um
G
Percent Proliferating Tumor Cells By Structure
Percent Proliferating Tumor Cells By Structure (per patient)
%KI67+PANCK+/PANCK+
ns
Perineural Invasion
Tumor
Tumor
Perineural Invasion